JGR Planets

RESEARCH ARTICLE
10.1029/2023JE007965

Unraveling the Tectonic History of the Tharsis Rise on Mars: Plume Migration and Critical Taper Dome

Oguzcan Karagoz[1], **Thomas Kenkmann**[1], **and Stefan Hergarten**[1]

[1]Institute of Earth and Environmental Sciences (Geology), Albert-Ludwigs-University Freiburg, Freiburg, Germany

Key Points:

- The study conducted a detailed mapping of concentric wrinkle ridges, which have 34,741 segments with a total length of 77,294 km
- The detachment depths ranging from 8.8 to 2.9 km are interpreted as a critical taper with a tectonic push induced by the Tharsis rise
- We identified five different causal stress centers, and the final stage of plume stress is transmitted toward Phoenicis Lacus

Correspondence to:

O. Karagoz,
oguzcan.karagoz@geologie.uni-freiburg.de

Citation:

Karagoz, O., Kenkmann, T., & Hergarten, S. (2024). Unraveling the tectonic history of the Tharsis rise on Mars: Plume migration and critical taper dome. *Journal of Geophysical Research: Planets*, *129*, e2023JE007965. https://doi.org/10.1029/2023JE007965

Received 20 JUN 2023
Accepted 20 DEC 2023

Author Contributions:

Conceptualization: Oguzcan Karagoz, Thomas Kenkmann
Data curation: Oguzcan Karagoz
Formal analysis: Oguzcan Karagoz
Investigation: Oguzcan Karagoz
Methodology: Oguzcan Karagoz, Stefan Hergarten
Project Administration: Oguzcan Karagoz
Resources: Oguzcan Karagoz
Software: Oguzcan Karagoz
Supervision: Thomas Kenkmann, Stefan Hergarten
Validation: Oguzcan Karagoz, Stefan Hergarten
Visualization: Oguzcan Karagoz
Writing – original draft: Oguzcan Karagoz

Abstract Wrinkle ridges are widespread tectonic landforms that serve as paleo-strain and paleo-stress indicators of the compressional history and thermal evolution of Mars. To reconstruct the center of the Tharsis rise and its migration with time, we mapped wrinkle ridges in the periphery of the dome and analyzed 34,741 wrinkle ridge segments with a total length of 77,294 km. We determined the deviation of each wrinkle ridge segment from a concentric strike direction for systematically changing centers. A fitting procedure indicates that all wrinkle ridge segments can be allocated with good precision to five different stress centers (C1-5) within the Tharsis rise: the southern edge of the Alba Mons caldera (C1), Ceraunius Fossae (C2), between Ulysses Patera and Pavonis Chasma (C3), Phoenicis Lacus (C4), and Claritas Rupes (C5). We performed a morphometric analysis of each wrinkle ridge and calculated the amount of shortening and depth of detachment, making use of methods for constructing balanced cross-sections. The amount of horizontal shortening varies from 1.5 to 3.8 km and the range of the detachment depth was found to be between 2.9 and 8.8 km, with significant variance forming an acute wedge of 1.2°–2.2°. Based on the critical taper theory, we inferred a very low basal friction coefficient ranging from 0.077 to 0.093 across the detachments for the five centers (C1–C5). Our findings suggest that these detachments are either localized along salt or clay layers or occur where liquid water is dominant below an impermeable permafrost layer.

Plain Language Summary Our study investigates wrinkle ridges on Mars in the area of the Tharsis rise, which is a huge volcanic bulge. Wrinkle ridges are compressive tectonic landforms that can reveal information about the planet's tectonic history and evolution. We mapped and analyzed thousands of such wrinkle ridges and used the results to identify the stress centers that caused the wrinkle ridge formation. We identified five different stress centers in the central region of the Tharsis rise, and we used simple balanced cross-sections to quantify the amount of radial shortening and the depth of detachment that occurred during Tharsis doming. We discovered that there was less friction than expected along the detachments, which may be due to the presence of water pressure or the existence of salt or clay layers lubricating the detachment shear planes. We evaluated the spatial-temporal position of the plume beneath the Tharsis rise and discussed its migration with time.

1. Introduction

The Tharsis region on Mars is a prominent volcanic province consisting of a broad, elevated topography, also referred to as the Tharsis rise. It has a diameter of roughly 6,000 km and a height exceeding 20 km (Scott & Tanaka, 1986). The formation of Tharsis has been undergone over the past 4 billion years, and it was volcanically active throughout the Late Amazonian period until less than 10 million years ago (e.g., Carr & Head, 2010; Dohm, Ferris, et al., 2001; Dohm et al., 2008; Hauber et al., 2011; Richardson et al., 2021; Robbins et al., 2011). This prolonged volcanic activity has resulted in the formation of numerous large and small volcanoes (e.g., Bleacher et al., 2007; Plescia, 2004; Richardson et al., 2021). In the Late Noachian (~4–3.7 Ga) to Early Hesperian (~3.7–3.1 Ga), the large volcanoes Alba, Olympus, Syria Mons, Arsia, Pavonis, and Ascraeus Mons have grown in the Tharsis area (e.g., Dohm, Ferris, et al., 2001; Dohm, Tanaka, & Hare, 2001; Nimmo & Tanaka, 2005; Phillips et al., 2001). The continuous accumulation of volcanic materials created a dome-shaped topography of the entire Tharsis region, which descends toward the edge of the Martian dichotomy. The prevalently agreed hypothesis for the formation of the Tharsis volcanic province is the presence of a mantle plume beneath the lithosphere (e.g., Breuer et al., 1996; Harder & Christensen, 1996; Hartmann, 1973; Kiefer, 2003; Roberts & Zhong, 2006; Solomon et al., 2005), while a superplume origin similar to those of Earth has also been proposed (Baker et al., 2007; Dohm et al., 2007). The way the topography of the Tharsis rise correlates with its gravity anomaly indicates deep-seated mantle processes (Harder & Christensen, 1996). Earlier studies proposed that

Writing – review & editing: Oguzcan Karagoz, Thomas Kenkmann, Stefan Hergarten

the Tharsis rise has been formed by a combination of isostatic uplift followed by flexural loading, the accumulation of volcanic deposits through a thin lithosphere, and crustal thickening through intrusion (e.g., Banerdt et al., 1982; Solomon & Head, 1982; Thurber & Toksöz, 1978; Willemann & Turcotte, 1982). Likewise, mantle convection models have been proposed to explain the crustal thickness and volcanic activity of the Tharsis area (e.g., Breuer et al., 1998; Harder & Christensen, 1996; Keller & Tackley, 2009; Mège & Masson, 1996a; Roberts & Zhong, 2006; Watters, 1993; Zhong & Zuber, 2001).

It has been recognized that the volcanic activities and the center of the Tharsis rise have shifted over time. Various conceptual studies have been conducted to explain the migration sequence of plume-induced stress centers and early migration of Tharsis volcanism from the southern latitudes toward the equator (e.g., Anderson et al., 2001; Frey et al., 1979; Hynek et al., 2011; Johnson & Phillips, 2005; Mège & Masson, 1996b; Wenzel et al., 2004; Zhong, 2009).

While Frey et al. (1979) suggests that the complex rift valley system of Valles Marineris, in conjunction with the orthogonal systems Echus and Juventae, can be attributed to episodic crustal warping, Dohm et al. (2009) present evidence for why the central part of the Martian canyon system was uplifted due to a Tharsis-related plume. The primary uplift event occurred in the Thaumasia region, giving rise to the Lunae Planum volcanic features, and establishing a north-south structural pattern. Subsequently, this pattern was superimposed upon and partially responsible for the formation of the east-west canyons in Valles Marineris, as well as the volcanic inundation of Solis Planum and Tharsis Plains. Mège and Masson (1996b) conducted a study of the plume tectonics models, and they interpreted dyke swarms on Solis Planum, which might compare to an early stage of plume rising, indicating the onset of a major Syria Planum plume. Anderson et al. (2001) proposed that the Tharsis volcanic center migrated from southern latitudes (e.g., Thaumasia and Claritas regions) to the dichotomy boundary during the Noachian epoch, as evidenced by structural analyses of radial features. Johnson and Phillips (2005) conducted a study on the distribution of magnetic field anomalies within the Tharsis region. They posited that the primary Tharsis magmatism was likely intrusive in nature, with the potential for an uplifted magnetized basement. Additionally, they suggested the presence of a pre-Tharsis crust, where Noachian units such as Claritas Fossae could signify either the initial Tharsis crust or the earliest Tharsis volcanic activity. Wenzel et al. (2004) demonstrated that the increased crustal thickness in the southern highlands could instigate mantle upwelling plumes beneath the thickened crust, as a result of its insulating properties. Conversely, Zhong (2009) advocated for a Tharsis mantle plume origin that developed and migrated beneath a lithospheric keel and the thickened crust, extending from the southern highlands to the crustal dichotomy boundary. Hynek et al. (2011) proposed that volcanic resurfacing near the south pole, which could be plausibly connected to Tharsis volcanism, may have originated in the vicinity of the present south pole and extended toward the equator. Leone (2016) indicated distinct global-scale volcanic alignments in its southern hemisphere, suggesting the presence of multiple mantle plumes rather than a single one.

2. Wrinkle Ridges Around Tharsis

Compressional and extensional landforms resulting from lithospheric deformation on Mars provide clues to its thermal and tectonic evolution (e.g., Banerdt et al., 1982; R. A. Schultz, 1985; Sleep & Phillips, 1985; Watters & Maxwell, 1983). Here we focus on wrinkle ridges, a widespread morphotectonic feature that predominantly occurs on volcanic plains (Knapmeyer et al., 2006, 2008) and results from the shortening of the upper crust as a consequence of compressive stresses (Watters, 1988). The Tharsis wrinkle ridge system surrounds the regional topographic center of northern Syria Planum and the main Tharsis volcanoes (Watters & Maxwell, 1986), and wrinkle ridges are also documented in the Northern Plains (Head et al., 2002). Tanaka et al. (1991) proposed a model in which the Tharsis lithosphere comprises a relatively thin elastic crust atop a robust, mechanically separated upper mantle. This model infers that deformation on faults beneath wrinkle ridges may propagate through the brittle crust and that the global compressional stress field is due to rapid planetary cooling and contraction. The uneven distribution of concentric tectonic features around Tharsis was explained by the localization of stress and strain near less robust volcano-tectonic centers (Tanaka et al., 1991). The circum-Tharsis wrinkle ridges occur most frequently in "ridged plains materials" that are thought to be from the Early Hesperian age (Watters, 1993). Dohm and Tanaka (1999) indicated wrinkle ridges formed both before and after the Early Hesperian (Scott & Tanaka, 1986), suggesting that the development of wrinkle ridges occurred over an extended period of time (Dohm & Tanaka, 1999). Wise et al. (1979) and Watters (1993) proposed that the wrinkle ridges are

not concentric around a single point on the Tharsis rise. There are two elongated concentrations of wrinkle ridges, one stretching from 15°S/95°W to 4°N/125°W, and a second, smaller elongated area is centered around 20°N and ranging from 40° to 70°W, which may indicate several centers. Further studies (Head et al., 2002; Mangold et al., 2000) proposed that the wrinkle ridges are Early Hesperian to Late Hesperian (Mangold et al., 2000) in age for Lunae, Solis, and Thaumasia Planum. In contrast, Anderson et al. (2001) proposed that wrinkle ridges formed around Tharsis from the late Noachian to the Early Hesperian indicate a primary center of stress at 4°S, 107°W based on their analysis. Again, other ages of wrinkle ridges and other compressional structures in the Tharsis region have been determined by Bouley et al. (2018) by using the ages and stratigraphy of the underlying geologic units. They classified them into six periods, ranging from Early Noachian to Late Amazonian. A recent study by Andrews-Hanna and Broquet (2023) reveals the presence of a significant peak in compressional strain during the late Noachian and early Hesperian periods (3.7 Ga–3.1 Ga).

Wrinkle ridges are common compressional structures with positive relief up to hundreds of meters that exhibit a linear or sinuous arch-like topography and may occasionally be overlain by smaller crenulated ridges (Watters, 1988). The formation of wrinkle ridges is still a topic of contention, with various theories including thrust-induced buckle folding, shallow subsurface thrust faults, fault propagation folding models and blind thrust models (Karagoz et al., 2022a; Mangold et al., 1998; Montési & Zuber, 2003; Okubo & Schultz, 2004; Schultz, 2000; Suppe & Connors, 1992; Watters, 2004; Yin & Wang, 2023). The key to understanding the wrinkle ridge formation is to obtain knowledge of faulting and folding of the subsurface of these structures. This critical information is sparse. These constraints make it challenging to obtain a comprehensive and unbiased collection of faults on a global scale. Anderson et al. (2001) investigated over 4,554 wrinkle ridges underpinned by compressional faults using images from the Viking missions. Knapmeyer et al. (2006) introduced a list of about 8,500 compressional faults on Mars using MOLA data from the Mars Global Surveyor mission. This database of Martian surface faults was updated to 1,409 additional compressional faults (Knapmeyer et al., 2008). Karagoz et al. (2022b) used impact craters, depressions, and valley cuts to obtain critical insights into the subsurface and could measure the dip of wrinkle ridge related reverse and thrust faults.

Among the numerous studies that have been completed on various aspects of the geologic and tectonic history of Tharsis, it was widely stated and accepted that plume-induced stresses were in approximate agreement with the distribution and orientation of compressive wrinkle ridge landforms (Anderson et al., 2001; Watters, 1993; Wise et al., 1979). However, as outlined above, the spatial-temporal position of the plume and the position stress centers beneath the Tharsis rise are not yet fully understood.

The objective of this study is a rigorous quantitative analysis of wrinkle ridges to narrow down the plume and stress history of Tharsis and gain further insight into the evolution of the Tharsis volcanic province. Building upon our previous morphometric analysis of wrinkle ridges (Karagoz et al., 2022a, 2022b) we investigate all circum-Tharsis wrinkle ridges (34,741 wrinkle ridge segments of 2 km intervals, with a total length of 77,294 km). We apply a method known as the "concentric deviation approach" (Poelchau & Kenkmann, 2008) and combine it with a novel fitting procedure to find best-fit stress centers based on wrinkle ridge analysis. The history of possible migration of the stress centers and plume activities is reconstructed by analyzing the superposition of branching or crosscutting wrinkle ridges. It is worth noting that this study does not encompass the assessment of relative age dating for each structure or the examination of their integrated stratigraphy.

3. Methodology

3.1. Data

To map wrinkle ridges on Mars, we used the NASA Planetary Data System (PDS) as a data source. The Mars Global GIS data set from the PDS was downloaded and implemented in ESRI ArcGIS Software. We employed the MOLA-HRSC blend mosaic (200 m/px) (Fergason et al., 2018) as the highest global resolution data set available, and the Thermal Emission Imaging System (THEMIS) daytime infrared mosaic (~100 m/px) as a base map (Edwards et al., 2011). It should be noted that the digital elevation data set of the MOLA-HRSC blend mosaic for some study areas (e.g., Lunae Planum) does not have an interim product with a resolution of 200 m/px (Fergason et al., 2018) and does not represent a compromise resolution of HRSC DEMs (~50–~100 m/px). Therefore, the Mars Orbiter Laser Altimeter (MOLA) resolution (463 m/px) (Smith et al., 2001) is preferred in these areas. We used fully controlled Mars Reconnaissance Orbiter Context Camera global image mosaics (Robbins et al., 2023)

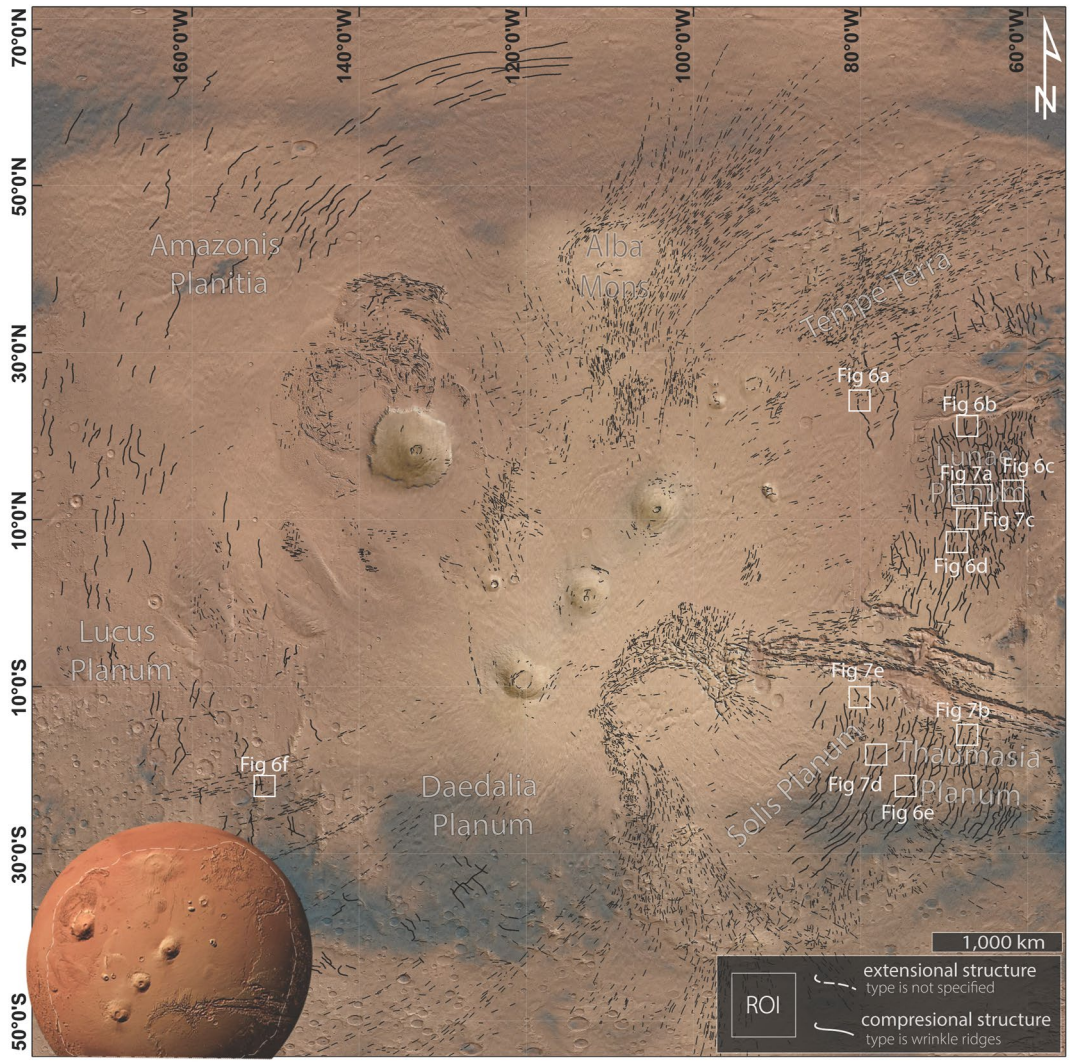

Figure 1. The global distribution of compressional (concentric) and extensional (radial) features in the vicinity of Tharsis is shown. The solid black lines represent compressional structures classified as wrinkle ridges, which are related to the Tharsis rise. The dashed black lines represent tensile cracks and rift structures without any distinction. The squares on the map indicate the Regions of Interest (ROIs), which are referenced later in Figures 6 and 7. Panels (a–f) display the areas where the cross-cutting relationships of wrinkle ridges are analyzed.

(CTX) (~6–7 m/px) in addition to the Thermal Emission Imaging System (THEMIS) daytime infrared mosaic to map wrinkle ridges and assess crosscutting relationships of ridges.

3.2. Mapping and Morphometric Analysis

In this study, we analyze 650 wrinkle ridges with a total length of 77,294 km that are all located in the periphery of the Tharsis rise and surround it in the western hemisphere of Mars (between 90°N and 90°S and 0°–180°W) (Figure 1). We based our analysis on the global fault catalog by Knapmeyer et al. (2006, 2008), which was assembled using MOLA data and considering two distinct illumination angles (45° and 315°). Owing to its rather low resolution, we were unable to extract the necessary wrinkle ridge segments for our analysis. Therefore, we mapped, digitized, and characterized wrinkle ridges (Karagoz et al., 2023) using high-resolution stereographic imagery at a scale of 1:5,000 from a CTX mosaic. Our mapping includes some buried wrinkle ridges in the Northern Plains, identifiable within the limits of the resolution offered by current topographic and stereo data sets. To exclude ridges affected by local deformation events (e.g., impact cratering), we used CTX imagery to distinguish the type of deformation. Specifically, we did not consider ridges with almost circular morphology, as they were

most likely formed by the filling and loading of flood basalts inside ghost craters by large azimuthal compressive surface stresses leading to subsidence and bending of the elastic lithosphere (Solomon & Head, 1980). To simplify the analysis, we mapped the crest line of the wrinkle ridges and segmented the data into 2 km intervals (1/5 for the shortest wrinkle ridge), which were then compiled into a spreadsheet for numerical analysis (Karagoz et al., 2023).

To perform the morphometric analysis, we computed several elevation profiles for each of the 34,741 segments using MATLAB software with the global HRSC-MOLA blended DEM (Fergason et al., 2018). We created a function that takes systematic elevation profiles perpendicular to the mapped segment line with a defined length toward both sides of the midpoint of the *x*–*y* reference pair. These profiles were used to measure the mean width and height of each circum-Tharsis wrinkle ridge (see Karagoz et al., 2022a for more information). This allowed us to calculate horizontal shortening and detachment depths using kinematic balancing approaches based on the conservation of the area of a two-dimensional cross-section perpendicular to the strike of the wrinkle ridges. To perform this approach, we used the assumption that the deformation pattern is purely concentric. While the exact sources and locations of the stress remain unknown, our investigation centers on the hypothesis that all wrinkle ridges converge concentrically to a common center. Therefore, we performed a quantitative analysis of the great circle plane concentric deviation, as described in the following section.

3.3. Concentric Deviation Analysis on a Sphere

We modified the "concentric deviation" approach developed by Poelchau and Kenkmann (2008) to analyze the orientation of wrinkle ridge segments with respect to potential stress centers. This analysis investigates the strike of structural data, for example, crestlines of wrinkle ridges, with respect to a single point and translates the geographic coordinate system with latitude/longitude notations into a radial system. The strike is then expressed as the deviation from concentricity with respect to a pre-determined center. This concept was previously applied in impact crater studies (e.g., Kenkmann et al., 2011).

Here, the initial approach is modified because the area of investigation is so large spanning 8,000 km, is so large that the spherical shape of the surface has to be taken into account. The approach is formulated in Cartesian coordinates on a unit sphere. Let, $\vec{a_i}$ and, $\vec{b_i}$ be the starting and end points of the segments, and

$$\vec{d_i} = \frac{\vec{a_i} + \vec{b_i}}{2} \tag{1}$$

is the respective middle point. We then consider a given center $\vec{c}$ on the unit sphere. The segment i is concentric with respect to c if the plane spanned by the vectors $\vec{a_i}$ and, $\vec{b_i}$ is normal to the plane spanned by the vectors $\vec{c}$ and $\vec{d_i}$. Otherwise, the cosine of the angle between the two planes describes the deviation from concentricity. This angle is obtained from the angle between the respective normal vectors $\vec{n_i}$.

$$\vec{n_i} = \frac{\vec{c} \times \vec{d_i}}{|\vec{c} \times \vec{d_i}|} \tag{2}$$

and

$$\vec{n_i'} = \frac{\vec{a_i} \times \vec{b_i}}{|\vec{a_i} \times \vec{b_i}|}, \tag{3}$$

where $\times$ is the vector product. Then,

$$\cos\,\alpha_i = \vec{n_i} \cdot \vec{n_i'} \tag{4}$$

The total quadratic deviation of all segments is then given by

$$F(c) = \sum_i (\cos\,\alpha_i)^2 = \sum_i \left(\vec{n_i} \cdot \vec{n_i'}\right)^2 \tag{5}$$

The root mean square angle (δ_{RMS}) can be determined by

$$\delta_{\mathrm{RMS}} = \sin^{-1}\left(\sqrt{\frac{F(c)}{N}}\right), \tag{6}$$

where N is the total number of segments.

The best-fit center c is then found by minimizing $F(c)$ numerically. Since c must be on the unit sphere, it is convenient to express $\vec{c}$ in terms of its longitude λ and latitude ϕ,

$$\vec{c} = \begin{pmatrix} \cos\phi\cos\lambda \\ \cos\phi\sin\lambda \\ \cos\phi \end{pmatrix} \tag{7}$$

Then the best-fit center is obtained by a two-dimensional minimization of F with respect to λ and ϕ.

It should be noted that the function to be minimized (Equation 5) contains no specific weighting. Since all considered segments have the same length, the minimization is implicitly weighted by the ridge length. Concerning the reconstruction of a stress field in a given region, weighting by area may theoretically be better than weighting by length. This would be possible by assigning a representative surface area to each ridge. It would, however, make the approach more cumbersome and would require further assumptions, for example, about a maximum area per segment. In order to keep the approach as simple as possible, we introduced no specific weighting, being aware that regions with a high density of ridges have a strong effect on the results. The procedure can be generalized to multiple centers, $c_1, \ldots, c_n$, assuming that each segment of the ridges is assigned to the center with the lowest concentric deviation.

We then have to consider

$$\overrightarrow{n_{ij}} = \frac{\overrightarrow{c_j} \times \overrightarrow{d_i}}{|\overrightarrow{c_j} \times \overrightarrow{d_i}|} \tag{8}$$

and

$$\cos\alpha_i = \min_j n_{ij} \cdot n_i' \tag{9}$$

The minimization can be performed iteratively. Starting from a random set of centers, each segment i is assigned to the center j that yields the lowest deviation $n_{ij} \cdot n_i'$ at first. Then, the location of each center is recomputed in such a way that it yields the minimum deviation F with regard to the segments assigned to this center. This procedure is repeated until the assignment of the segments to the centers does not change anymore. However, this iterative scheme has a tendency to get stuck at local minima of F. Therefore, a large number of initial configurations (locations of the centers) have to be simulated in order to obtain the globally best solution.

It should be noted that the term "center (C)" refers to a geometric center of the stress field that is computed purely on a mathematical approach. The defined centers labeled C1 to C5 are distributed in both the northern hemisphere and the southern hemisphere of Mars. Unraveling the sequential activation of the causative stress centers is based on the observation of the cross-cutting relationships and superposition of circum-Tharsis wrinkle ridges.

3.4. Detachment Depth

We assume that wrinkle ridges are formed by fault-propagation folding (see Karagoz et al., 2022b to consider different formation models) and use the Suppe and Medwedeff (1990) model to simulate and balance an iso-volumetric plane-strain deformation. The balancing approach is detailed in Karagoz et al. (2022a) and calculates the amount of shortening and the depth of the detachment from the measurable width and height of the wrinkle ridges and the dip of the fault ramp underneath the wrinkle ridge. We considered a constant dip angle of 37° for the ramp based on measurements (see Karagoz et al., 2022b). This model is suitable for the formation of asymmetric folds with limbs of different dips due to the propagation of a thrust fault beneath the fold. The growth of the fold is self-similar and occurs through kink-band migration, with its shape and position preserved relative to the propagating fault tip.

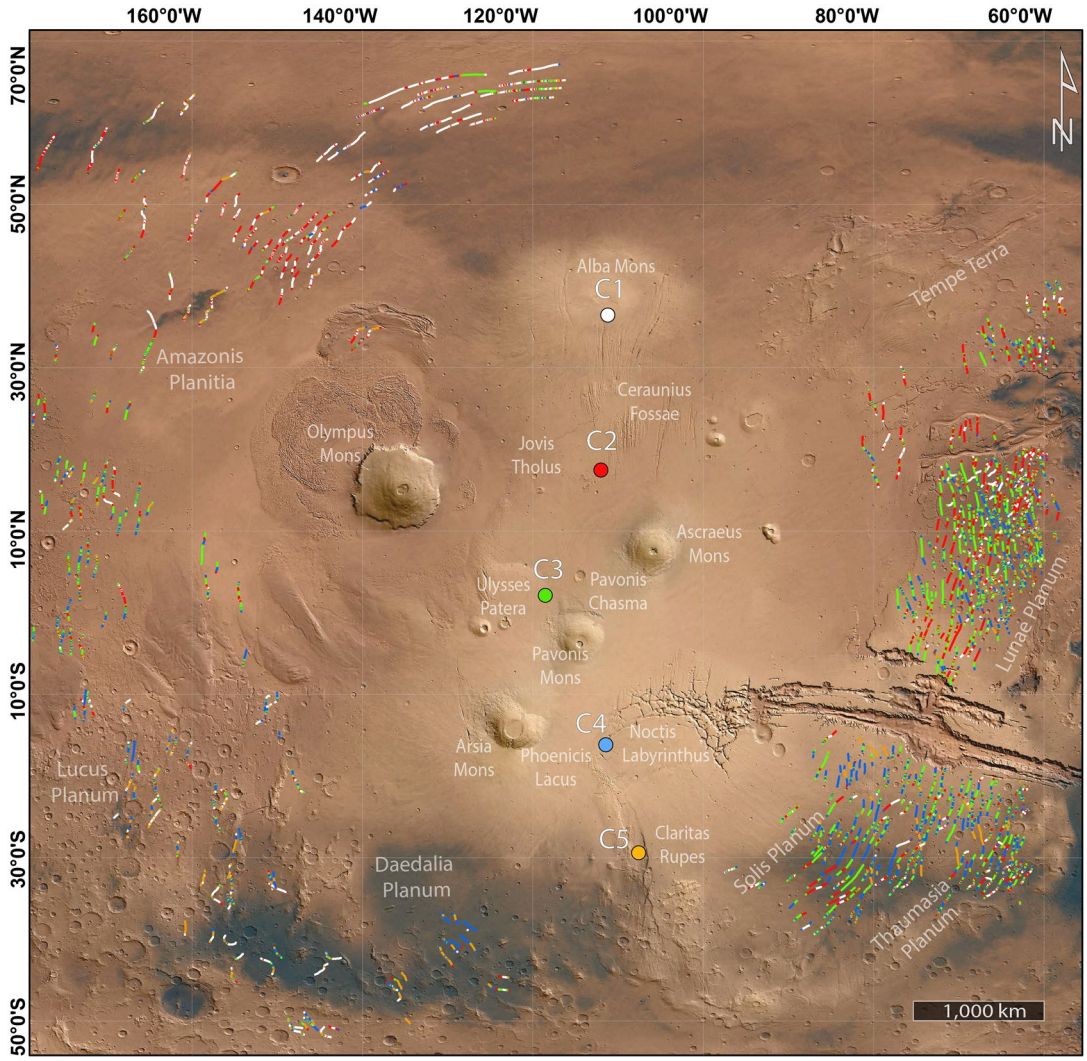

Figure 2. The distribution of examined circum-Tharsis wrinkle ridges for a 2 km segment interval and their associated stress centers were calculated using the concentric deviation method from centers C1 to C5. The corresponding centers and segments are given in the same colors. The authors refer to the color version of this and all subsequent figures.

We obtained the best-fitting locations of the stress centers and displayed the calculated detachment depth with radial distance from the stress centers to the Tharsis periphery. For each wrinkle ridge segment assigned to a specific center (C), we depicted the detachment depth and corresponding topographic elevation in relation to their radial distance from the center. The data were subsequently averaged, and linear regression was computed for each of the designated centers.

Table 1
The Quantitative Analysis of Horizontal Shortening for Ridge Segments in Five Geological Centers (C1 to C5)

Centers	Minimum amount of horizontal shortening (M) on ridge segments	Maximum amount of horizontal shortening (M) on ridge segments	Horizontal shortening (KM) of ridges on radial profile
C1	20.1	53.8	1.5
C2	38.6	62.6	2.9
C3	28.4	94.7	3.6
C4	36.5	107.5	3.8
C5	19.4	57.2	1.7

4. Results

4.1. The Results of Planar Concentric Deviation Analysis

Our analysis of concentric deviation shows that five different stress centers cover almost all wrinkle ridges of the Tharsis rise with satisfying precision. They are denoted as C1 to C5 (Figure 2) (Table 1). In Figure 3a, the center C1 (35.67°N, 110°W) at the 5105.5 m altitude is found at the southern edge of the Alba Mons caldera, and it corresponds to the strongly aligned point among the 4,140 white-colored segments between Arcadia Planum and the

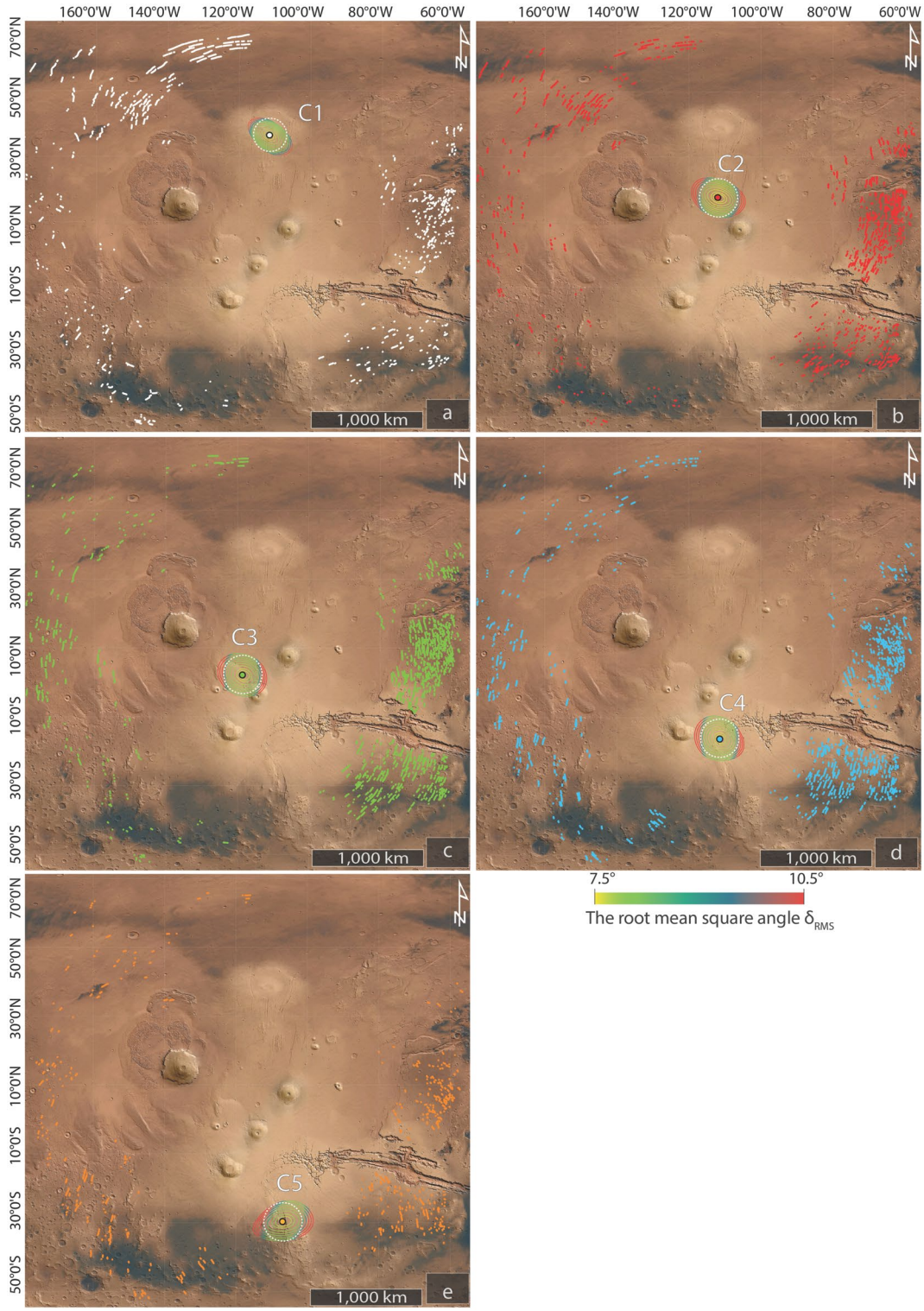

Figure 3. (a) The center C1 corresponds to the best-fit point at the southern edge of Alba Mons for the white-colored segments. (b) The center C2 is located between Jovis Tholus and Ceraunius Fossae for the red-colored segments. (c) The center C3 and the green segments are given; they fit between Ulysses Patera and Pavonis Chasma. (d) Center C4 is the best-fit point at Phoenicis Lacus in the western part of Noctis Labyrinthus for the blue segments. (e) The center C5 is positioned at the Claritas Rupes region and is represented using orange-colored segments. The contour lines for each center from C1 to C5 demonstrate the deviation in the computation of the quantitatively best-fitting stress centers.

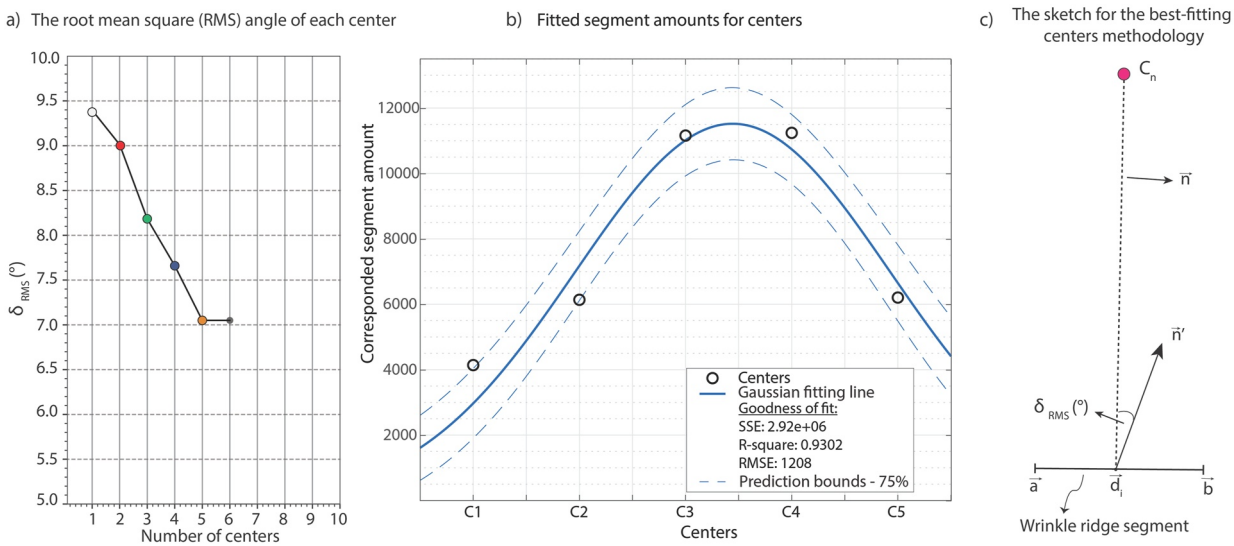

Figure 4. (a) The diagram illustrates how the root mean square angle (δ_{RMS}) changes as the number of centers increases during the calculation for the best-fitted centers using the great circle plane approach on concentric deviation. The deviation stabilizes after computing the fifth center. (b) The quantities of segments used for calculating the located centers (C1–C5) are presented, and their distribution likely indicates a symmetric, bell-shaped normal distribution. (c) The simplified sketch shows the calculation best fitting centers with respect to the root mean square angle (δ_{RMS}).

northwest of the Tharsis rise, as well as in the eastern part of Lunae Planum. In Figure 3b, center C2 (18.50°N, 111.53°W) at 3011.8 m is situated between Jovis Tholus and Ceraunius Fossae. The C2 center is indicated by 6,137 red segments distributed from Arcadia Planum to the south of Daedalia Planum in the west and more densely from Tempe Terra to Solis Planum in the east. In Figure 3c, the center C3 (4.44°N, 115.67°W) corresponds to the highest topographic elevation between Ulysses Patera and Pavonis Chasma at 3,225 m altitude and is the common intersection point for 11,158 green segments. These segments are mostly located to the east of the Tharsis rise, with a significant concentration in Lunae Planum, to the southeast in Solis Planum and Thaumasia Planum, and to the west in the less significant Amazonis Planitia. In Figure 3d, the center C4 (10.11°S, 110.57°W) is aligned at Phoenicis Lacus in the western part of Noctis Labyrinthus at 4,846 m altitude. This center point is where the blue-colored segments intersect, with 11,241 segments in total. The distribution of these segments is particularly dense in Solis Planum and Thaumasia Planum to the east and in Lunae Planum to the northeast. In Figure 3e, the center C5 (23.26°S, 106.18°W) is in the central Claritas Rupes region at 3,829 m altitude and is associated with 6,205 orange-colored segments that are oriented southeast to northwest and spread south of the Tharsis rise. The majority of wrinkle ridge segments correspond to centers C3 and C4. Figure 4a, shows that the computation of centers is fixed at five centers (where δ_{RMS} is constant), and the segment of the ridges does not correspond to any new center.

4.2. The Results of Shortening and Detachment Depth

The calculated amount of horizontal shortening, as derived from the application of our kinematic model approach (Karagoz et al., 2022a), is presented in Table 2. These computations are based on the mean height and width of each wrinkle ridge, pertaining to a comprehensive set of 34,741 wrinkle ridge segments. Each of these segments is uniquely associated with a center ranging from C1 to C5.

The reconstruction of C1 is based on 4,140 ridge segments, with shortening ranging from 20.1 to 53.8 m for each wrinkle ridge. C2, hosting 6,137 ridge segments, revealed a greater degree of shortening, with the lowest amount measured at 38.6 m and the highest reaching 62.6 m for each wrinkle ridge. C3, which accounted for the largest number of ridge segments (11,158), exhibited an extensive range of shortening ranging from 28.4 to 94.7 m. C4, with a slightly higher count of 11,241 ridge segments, showcased shortening measures from 36.5 to 107.5 m for individual wrinkle ridges. C5 included 6,205 ridge segments, with shortening values ranging from 19.4 to 57.2 m.

Our results demonstrate that the analysis of the 34,741 wrinkle ridge segments across the five centers indicated that the amount of horizontal shortening varied significantly. The horizontal shortening along the representative 4,000 km topographic radial profiles varied from 1.5 to 1.7 km.

Table 2
The Table Provides a Computed of the Results Derived From the Process of Determining Fitting Centers, Ranging From C1 Through to C5, Along With the Relevant Derived Data

Centers	Coordinates	Altitude of centers (m)	Amount of ridge segments	Geological location	The depth of detachment (km)	The average topography slope (α°)	R^2 of α fitting	RMSE of α fitting	Basal tilt (β°)	R^2 of β fitting	RMSE of β fitting	The basal friction coefficients μ_b
C1	35.67°N, 110°W	5105.5	4,140	The southern edge of the Alba Mons caldera	~8.2–2.9	0.83	0.969	0.711	0.97	0.919	0.664	0.0773
C2	18.50°N, 111.53°W	3011.8	6,137	Between Jovis Tholus and Ceraunius Fossae	~8.8–5	0.68	0.853	0.609	0.67	0.891	0.687	0.059
C3	4.44°N, 115.67°W	3,225	11,158	Ulysses patera and Pavonis Chasma	~7.8–4.8	0.62	0.796	0.902	0.65	0.831	0.317	0.0552
C4	10.11°S, 110.57°W	4,846	11,241	Phoenicis Lacus in the western part of Noctis Labyrinthus	~8–5.1	1.08	0.859	0.644	0.62	0.883	0.505	0.0782
C5	23.26°S,106.18°W	3,829	6,205	Claritas Rupes	~6.8–3.8	1.31	0.789	1.517	0.71	0.895	0.439	0.0934

Note. This assessment incorporates an evaluation of the basal tilt and surface slope angles which are acute parameters in the context of the incipient taper.

The results of the detachment depth derived from the kinematic model, based on the morphometric mean height and width of 34,741 segments of wrinkle ridges, are presented in Figure 5 as a function of distance to the respective center points (Table 2.).

In Figure 5a, the calculated detachment depths for center C1 range from approximately ~8.2–~2.9 km, measured from the respective elevation of the wrinkle ridge. A systematic trend is visible, with the detachment getting shallower away from the center and toward the periphery of the Tharsis dome. The R^2 value of the linear regression for the detachment values is 0.919. The distribution of depth-of-detachment values carries a margin of error of ±0.5 km, and the root mean square error (RMSE) of the fitting is 0.664. The average basal tilt angle (β) of the detachment was 0.97°. The radial cross-section also shows a swath of topographic data plotted with a radial range from center C1 (Figure 5a). The average topography angle (α) is 0.83°. The R^2 value of the linear regression for the average topography is 0.969, and the RMSE of the fitting is 0.664.

Figure 5b displays the calculated detachment depths for center C2, ranging from approximately −8.8 km to −5 km. The detachment depth remains largely constant in the vicinity of 1,500 km from the calculated center C2 before ascending to shallower levels. An additional kink in the detachment slope occurs at around 2,100 km. Beyond this point, a constant increase in the depth of the detachment is observed. Linear regression analysis revealed an R^2 value of 0.891, and a derived basalt tilt (β) of 0.67°. The detachment depth values exhibited a margin of error of ±0.45 km and a root mean square error (RMSE) of 0.664. The radial topographic swath profile from center C2 (Figure 5b) shows kinks at approximately 2,500 km and 3,250 km with an average slope angle (α) of 0.68°, an R^2 value of 0.853, and an RMSE of 0.609 for the fitting.

Figure 5c presents the detachment depth results for center C3 as derived from the assigned wrinkle ridge segments. The detachment depth increases from approximately −7.8 km near center C3 to −4.8 km at a distance of 4,000 km from C3. A distinct kink in the dip of the detachment occurs at a distance of 3,000 km. Linear regression analysis indicates an R^2 value of 0.831, and a calculated basalt tilt angle (β) of 0.65°. Detachment depth values exhibit a minor margin of error <±0.35 km and an RMSE of 0.3137. The topographic swath profile reveals a systematic decline in elevation from the stress center with an average slope angle (α) of 0.62° and a kink in the slope starting at 2,750 km. The R^2 value for the linear regression of the average topography is 0.796, and the RMSE for the fitting is 0.902.

Figure 5d demonstrates the detachment depth and elevation results for center C4 at Labyrinthus Noctis, obtained by utilizing the relevant 11241 wrinkle ridge segments. The figure depicts a gentle rise of the detachment depth from roughly −8 km to −5.1 km with increasing radial range, while the topography exhibits a gentle outward dip from center C4. The detachment results and topographic profile both show distinct kinks at 2,500 km. A basalt tilt angle (β) of 0.62° and an average topography angle (α) of 1.08° were calculated as the distance from C4 grows. Linear regression analysis of the detachment data yielded an R^2 value of 0.883. The detachment depth values

10.1029/2023JE007965

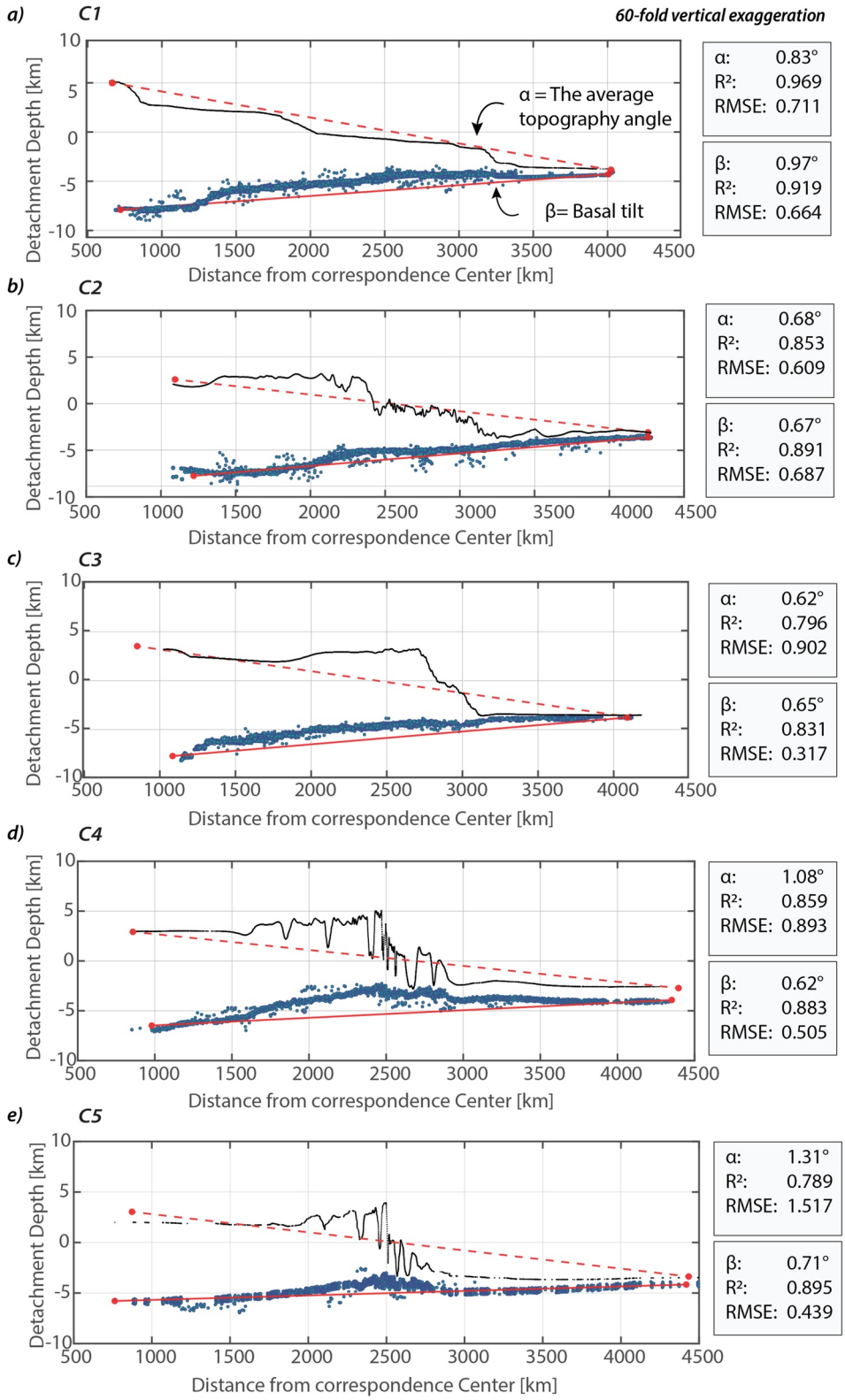

Figure 5. Schematic diagrams (a) through (e) display the detachment depth results (represented by blue dots) for different wrinkle ridge segments with their respective centers ranging from C1 (a) to C5 (e). These results were obtained using a kinematic modeling approach with a constant dip angle of 37° (refer to Karagoz et al. (2022a) for further information). The solid black line in each diagram represents the radial topographic swath profile for each respective center. The solid red line indicates the average slope of detachment, while the red dashed line represents the average surface slope. Here, β signifies the basal tilt angle, and α denotes the surface slope angle.

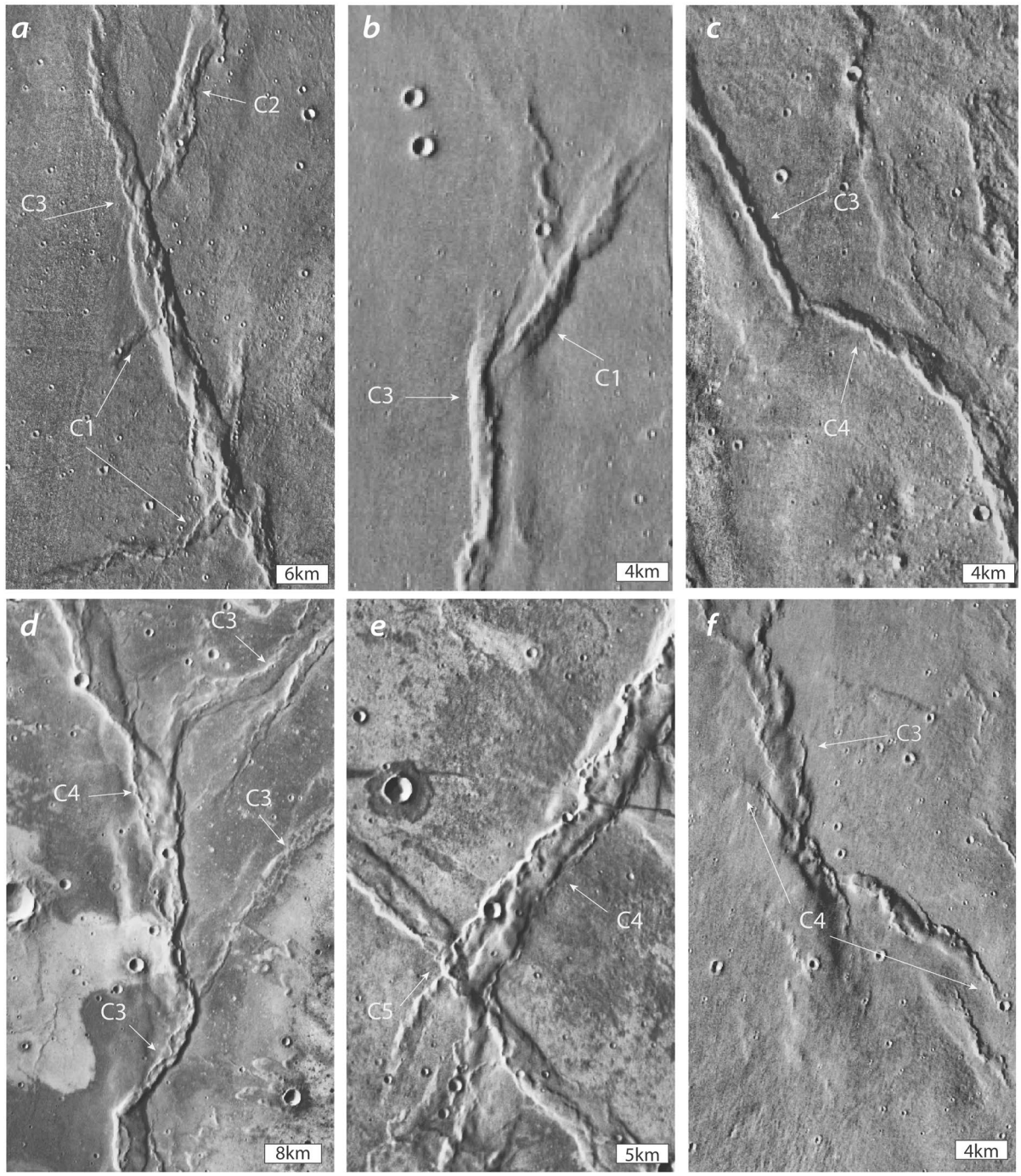

Figure 6. The figure shows examples of superposition relationships between the individual wrinkle ridges and the centers corresponding to the different segments (a–f) using the THEMIS IR day mosaic data set. (a) The C2 segment is cut by a straight strike from the comparatively symmetric ridge segment that belongs to C3. (b) The C3 center is overlapped by the C1 segment on the back limb of the ridge. (c) The tip of the C4 segment appears to be translated by C3. (d) The ridge segments corresponding to the C3 center are relatively shorter in thickness and are cut by the asymmetric ridge segment of the wider and higher C4 center. (e) The symmetrical segment of the C4 ridge cuts the asymmetrical ridge of the C5 center. (f) The relatively young asymmetric ridge corresponding to the C4 center cuts the asymmetric ridge segment of C3. The locations of observation are given as ROIs in Figure 1.

have a margin of error of ±0.55 km, and the RMSE is 0.505. The R^2 value for the linear regression of the average topography is 0.859, and the RMSE for the fitting is 0.893.

Detachment depths for center C5 (Figure 5e) are noticeably shallower. The detachment rises from −6.8 km to −3.8 km as the distance from C5 increases, with a calculated basalt tilt angle (β) of 0.71°. A kink toward a flat detachment

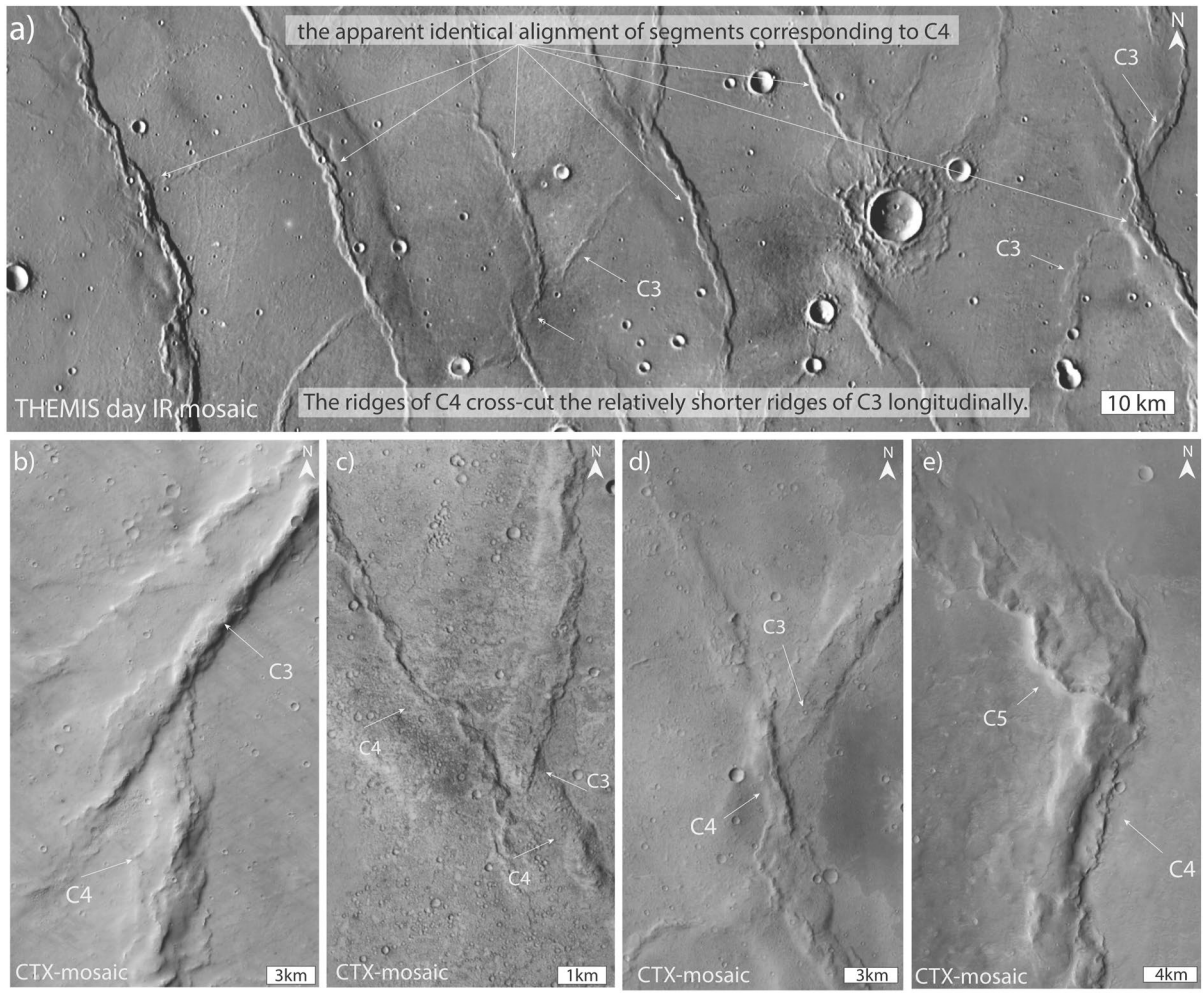

Figure 7. (a) The prevalent alignment and equal spacing between wrinkle ridge segments that corresponds to activation of C4 and C3 stress centers can be more considerably followed in Lunae Planum (14.74°N, −63.93°W). (b) The C4 segment appears to be superposed by a C3 segment. (c) The C4 segment is cut by a straight strike from the comparatively small ridge segment that belongs to C3. (d) The C3 segment is cut by a relatively fresh C4 segment. (e) The C5 segment visibly overlays the C4 segment.

was observed at approximately 2,500 km distance from the center C5. The slope of the topographic swath profile is steepest in this section. Linear regression analysis of the data yields an R^2 value of 0.895, with the detachment depth values having a margin of error of ±0.25 km and an RMSE of 0.439. The associated topography descends from the stress center and possesses an average slope (α) of 1.31°, transitioning to a flat topography at roughly 2,750 km. The R^2 value for the linear regression of the average topography is 0.789, and the RMSE for the fitting is 1.517.

5. Discussion

5.1. Stress Center and Plume Migration

The distribution of wrinkle ridges on the surface of Mars provides insights into the tectonic history of the Tharsis rise. We identified five different stress centers that are all located within the Tharsis rise and are distributed over 4,518 km from north to south. To reconstruct the migration history of the stress centers in the course of the geological history, we need to establish a sequence of their activation by the examination of superposition and cross-cutting of wrinkle ridges that belong to different stress centers (Figure 6). Figure 6a noticeably indicates that the asymmetric wrinkle ridge segment corresponding to the center C2 is cut with a straight strike by the comparatively symmetric ridge segment that belongs to C3, thus the segment allocated to C3 postdates the segment allocated to C2. The thrust front of the ridge segment is located in front of the ridge crest, where the maximum displacement is visible and is associated with subsidiary faults. The small C1 segments trend almost perpendicular to this and can be regarded as

the youngest element, cutting the segments belonging to the C3 and C2 centers. In Figure 6b, the ridge segment associated with the C3 center is overlapped by the C1 segment on the back limb of the ridge, confirming that the C1-related ridge is a relatively young thrust. In Figure 6c, the tip of the C4 segment appears to be translated by C3. In this case, the C3-related ridge is a younger wrinkle ridge structure than C4. Figure 6d shows examples of a multitude of intersections of wrinkle ridges and is likely a good example to demonstrate the reactivation of ridges. The ridge segments corresponding to C3 are relatively shorter in width and are cut by the asymmetric ridge segments of the wider and higher C4-related ridges. This contrasts with Figure 6c and confirms that the stress center that caused the formation of the ridges has changed through time. Figure 6e proves that the symmetrical segment of the C4 ridge cuts the asymmetrical ridge of the C5 center. The ridge is abruptly interrupted at the location of the C5 segment, but it is possible to follow the thrust front of the ridge associated with C4 with fewer vertical throws in the same strike direction. Figure 6f demonstrates that the asymmetric ridge segment of C3 is cut by a relatively young asymmetric ridge corresponding to the C4 center. The C4 stress center was activated at least two different times and was the last to be activated. Before the most recent activation of the C4 center, the C3 stress center completed its activity with one more repetition of surface stresses. In addition, limited observations of the intersection of the wrinkle ridge segments corresponding to the C2 center and the C1 center reveal that only the C1 ridge is younger than C2. In addition, although the C5 segment confirms the reactivation of the C4 segment, it doesn't provide enough information to relate this to other stress centers. The cross-cutting relationship between C3 and C4 is among the most prominent findings.

In Figure 7a, the dominant alignment of the wrinkle ridge segments associated with C4 seems to overlap the ridge segments that belong to C3. Alternatively, the differently oriented ridge systems might be formed in a single transpressive scenario. In Figure 7b, it appears that the C3 segment is superimposed on the C4 segment. Figure 7c also displays that segment C4 is cut by a smaller ridge segment from C3. In Figure 7d, the C3 segment is cut by a relatively fresh C4 segment. In Figure 7e, the C5 segment is clearly seen overlaying the C4 segment. If we put all superposition and crosscutting observations together and accept that differently oriented ridges are formed by various stress states so that plane strain conditions are always fulfilled, then we can derive the following sequence of events abbreviated by its stress center labels:

C2, C3, C1, C4, C3 (activated), C5, C4 (activated). To summarize this, we derive an overall shift of the Tharsis stress center from the northern to the southern location. However, this seems to be not a continuous migration but is interrupted by phases of backflipping and the simultaneous activation of several volcanic centers. This sequence can be related to previous analyses: Watters and Maxwell (1986) proposed that the Tharsis rise adheres to a trajectory in close proximity to the regional topographic center of the northern Syria Planum and the principal Tharsis volcanoes. Although our findings indicate the presence of multiple centers, it is noteworthy that C4 is situated near the Syria Planum.

Wise et al. (1979) and Watters (1993) proposed two elongated clusters of centers that stretch from 15°S, 95°W to 4°N, 125°W. These centers are closely located to C3 (4.44°N, 115.67°W), corresponding to the highest topographic elevation between Ulysses Patera and Pavonis Chasma, and C4 (10.11°S, 110.57°W) is aligned at Phoenicis Lacus in the western part of Noctis Labyrinthus in our findings. Based on the analysis of wrinkle ridges, Anderson et al. (2001) reconstructed that the primary stress center is at 4°S, 107°W. The location of this center is, in general, located in Noctis Labyrinthus and is closely in line with our findings of Phoenicis Lacus in the eastern part of C4 (10.11°S, 110.57°W). Anderson et al. (2001) analyzed the radial extensional features of the Tharsis rise from the Late Noachian to the Late Amazonian and identified centers for Alba Mons, Syria Planum, and the flank of Ascraeus Mons. These locations correlate with our stress center at C1, C4, and C3, respectively. A challenge is to determine the absolute ages of compressional and radial extensional features (Head et al., 2002; Mangold et al., 2000). Recently, Bouley et al. (2018) subdivided the ages of wrinkle ridges and other compaction structures in the Tharsis region into six periods ranging from the Early Noachian to the Late Amazonian. They suggested that compressional deformation has started in the eastern periphery of the Tharsis region, and subsequently shifted toward the Tharsis center from the West of Tempe Terra and Solis Planum. This shift could be considered to represent a tectonic in-sequence migration of deformation. Our findings are consistent with Bouley et al. (2018) with C1 in the south of Alba Mons, west of Tempe Terra, and C4 in Phoenicis Lacus. Andrews-Hanna and Broquet (2023) assert that while assigning age constraints to geological units, a tectonic structure can be of any age that is lower than the surfaces it intersects. Based on this, all circum-Tharsis wrinkle ridges should be formed between the Late Noachian and Early Hesperian.

We accept that the inferred stress centers are caused by thermal plumes and related topography. A mantle plume induces a rapid increase in topographic uplift and a positive geoid anomaly at the surface above the plume. The shift of stress centers indicates the migration of the underlying plumes within the area of the

Tharsis rise. Our results indicate a migration of the plume from north to south with phases of multiple and flipping plume activation. When a plume migrates, it can form branches (e.g., on Earth, Dongmo Wamba et al., 2023). It may be led by variations in the mantle's heterogeneity and by areas of low velocity, leading to the formation of vertical plume conduits and horizontal ponding zones. If the plume is moving toward the shallow weakened crust, the thickening of volcanic material and strength of the overlying lithosphere can control the branching of the plume. If the thick lithosphere cannot allow plumes to reach the surface, it may potentially cause activation on plume branches where the dichotomy boundary persists (and between C4 and C3). The changing mantle rheology due to volcanic outgassing and/or the presence of volatile compounds such as water or carbon dioxide can also influence the buoyancy and activity of the plume. That agrees with an abrupt decrease in the accumulated tectonic strain and strain rate after the early Hesperian (Andrews-Hanna & Broquet, 2023).

Different scenarios regarding the activity sequence of the stress centers can be considerable. If one disregards the cross-cutting evidence of C3 and C4 segments (observed in Figures 6c and 7b), it may simplify the sequence of events, thereby obviating the need for hypothesizing reactivation. While establishing a definitive spatial relationship between C5 and C1 may present challenges, the sequence from (C2 and C1) to C3 and then to C4 is discernible with clarity, ending on C5 (see Figure 7e). Another scenario is sequence as a result of C3 and C4 being persistent centers of activity with overlapping durations. This scenario accepts the consideration that multiple plumes may exist, which could be either independent or sustained by a singular, larger megaplume (e.g., Baker et al., 2007). Moreover, the substantial degree of shortening and the higher frequency of associated wrinkle ridges observed at C3 and C4 align with a scenario of prolonged activity, especially when compared to the lesser extent of activity at C1, C2, and C5. If we accept a single plume migration scenario, our findings suggest that the oldest volcanic material accumulation center is located at C2 and confirms the movement toward the C3 center with higher topography where Tharsis Montes is situated. Instead, the independent growth of Alba Mons caldera may have been caused by a small rising plume as a hotspot (previously proposed by Janle & Erkul, 1991) that acts as a horizontal surface stress, which could not contradict the scenario of moving single plume initiation. Despite this, all stress centers occurred parallel to and west of the Tharsis Montes. However, in the region southeast of Arsia Mons, the plume activity resulted in shallower depths near the C4 center at Noctis Labyrinthus. Our observations suggest reactivation phases of surface stress. If a single plume scenario is adequate, the plume tail should drive causative stress centers between C3 and C4, and eventually may be directed toward the occurrence of the C5 center, Claritas Rupes. This postpones the reactivation of the C4 stress center as the youngest stress center. Richardson et al. (2021) confirmed that within the most recent 500 Ma, magma was present under and to the east of the Tharsis Montes and built hundreds of small volcanoes in this region.

Contrary to previous studies, our results reveal that early migration of Tharsis volcanism from the southern latitudes toward the equator (Anderson et al., 2001; Frey et al., 1979; Hynek et al., 2011; Johnson & Phillips, 2005; Mège & Masson, 1996b; Wenzel et al., 2004; Zhong, 2009) or the vicinity of the present south pole and extended toward the equator (Hynek et al., 2011) might not be feasible. The transition of the plume over time is most likely a key phenomenon to understanding the rise of Tharsis due to a combination of isostatic uplift, flexural loading, the accumulation of volcanic deposits, and crustal thickening.

Our horizontal shortening results are evaluated through a detailed analysis of wrinkle ridge segments on radial topographic profiles, with the total count across all centers being 34,741 segments (Figure 4b). Each center, individually, reveals interesting trends and significant variation in the values of shortening. Center C1, with 4,140 segments, demonstrates the lowest range of shortening. However, the fact that it culminates in a horizontal shortening of 1.5 km is notable, indicating a considerable spread of independent deformation. Center C2, with a larger number of ridge segments (6,137), has a horizontal shortening of 2.9 km. C3, despite having a slightly lower number of segments (11,158) than C4, shows a lower horizontal shortening on a radial profile of 3.6 km. The center C4, with the largest number of ridge segments (11,241), exhibits horizontal shortening on a radial profile of 3.8 km. Notably, this suggests that C4, while hosting a maximum number of ridge segments, also experienced a high degree of deformation, as measured by the highest maximum shortening of 107.5 m for the ridge segment. This may suggest differences in the lithospheric instabilities of C4 that cause higher amounts of deformation per segment compared to C3. On the other hand, the C5 center, despite having a higher number of ridge segments (6,205) than C2, shows considerably less horizontal shortening along topographic profiles than C2 with 1.7 km.

5.2. Tharsis—A Critical Taper Dome?

The calculated detachment depth profiles for each stress center show clear trends toward shallower detachments with increasing radial distance. The present-day topography likewise shows a systematic descent with increasing radial range. This trend is observable at a distance of about 3,000 km to the respective stress center. Karagoz et al. (2022a) applied the principles of the critical taper theory (Dahlen, 1990) to the analysis of wrinkle ridges at Lunae Planum on Mars. Their proposition posits that both basal detachment and topography represent an incipient critical taper. This study supports these earlier findings that were restricted to a rather small area and indicates that the entire Tharsis rise follows this trend.

The critical taper theory was developed to understand the dynamics of foreland fold-and-thrust belts and accretionary prisms on Earth (Dahlen, 1990) both having a wedge shape geometry in a cross-sectional view. The theory is based on force balance considerations and predicts that a wedge-shaped geometry evolves toward failure equilibrium and grows in a self-similar manner. The critical taper concept assumes mechanical equilibrium between a compressional force (the tectonic push) that created the wedge and the resisting forces inside the wedge. More specifically, force balance is achieved when the detachment-parallel component of gravitational force, together with the resulting overburden pressure and basal shear traction, is equal to the compressive push from the rear. The angle of the critical taper (α surface slope and β basal tilt) depends on various factors such as the material properties within the wedge, the pore fluid pressure, and the friction properties of the detachment at its base. When applying this concept to the Tharsis rise, one has to consider that a two-dimensional wedge is replaced by a huge dome of 6,000 km in diameter. However, due to the sheer size of the dome, the shortening of individual wrinkle ridges can still be approximated by plane strain. Another variation concerns the rigid push from the rear that is replaced by the plume head.

Our basal detachment depth calculations show that the stress center C1 corresponds to the highest amount of basal tilt. Since the C1 stress center is located near the Alba Mons caldera, this result may be affected by Amazonian-aged volcanic material whose load may have pressed the detachment downwards after their formation. The maximum depth of detachment exists for the stress center C2. Center C2 is situated between Jovis Tholus, south of Cerauinus Fossae, and Jovis Tholus, beneath the volcanic materials of Ascraeus Mons. This location is likely the result of magma intrusions causing the topographic bulging and surface stresses from accumulated material. It may also represent a transition point from one stress center to another, assuming a single moving plume. It is observed that the slope angle of the basal detachment is reduced for the stress center C3. This is compensated for by a steeper relief slope in the vicinity of Pavonis Chasma. The C4 center is situated west of Noctis Labyrinthus in Phoenicis Lacus. The C5 center has the shallowest detachment depth and basal tilt angle in Claritas Rupes. The formation of this geological feature is more complex than it appears. The elongated Claritas bulge consists of two parallel major axial ridges separated by a trough. The elevated eastern footwall side of Claritas Rupes intersects an old highland in the middle. These tectonic stresses may be correlated with magma intrusions, resulting in a western axial set of oblique ridges or the formation of an extensive horsetail set of grabens.

5.3. Wedge Angles and Their Mechanical Implications

The wedges derived for the individual centers, as depicted in Figure 5, show a variation of the basal detachment that ranges between $\beta = 0.97°$ and $0.62°$. The wedge slopes vary from $\alpha = 0.62°$–$1.31°$. The wedge-shaped configuration shows certain similarities to Earth's accretionary wedges and foreland fold-and-thrust belts (for instance, von Hagke et al., 2014), despite their usual formation through extensive thrust and duplex systems with substantially greater displacement and larger taper angles of 2.5–12.5° (Saffer & Bekins, 2006). However, foreland fold-and-thrust belts exhibiting extremely small taper angles do exist, for example, in the Jura Mountains, Switzerland (see Table 2 of Karagoz et al. (2022a), for other examples).

The critical taper angle $(\alpha + \beta)$ (in radians) depends on the internal friction angle ϕ of the material involved in the taper and the basal friction coefficient μ_b of the detachment (Dahlen, 1990). In a mechanically homogeneous wedge, the critical taper equation, employing the small angle approximation of Dahlen (1990), is as follows:

$$(\alpha + \beta) \approx \frac{\beta + \mu_b(1 - \lambda_b) + S_b/\rho g T}{1 + 2(1 - \lambda_b)\left(\frac{\sin \phi}{1 - \sin \phi}\right) + C/\rho g T} \tag{10}$$

where ρ is the mean density of rock, g is the gravity, μ_b is the basal friction coefficient, λ_b is the basal pore fluid to lithostatic pressure ratio, S_b is the basal cohesion, C is the compressive wedge strength, ϕ is the angle of internal friction, and T is the wedge thickness.

The inclined basal detachments and the gentle slopes in topography are interpreted as incipient states of a critical taper with a very narrow taper angle. The horizontal tectonic push is provided by the lithospheric thickening and most likely by associated gravity-driven forces. The extremely gently rising basal detachment, the narrow taper angle, and the absence of clear vergence of the wrinkle ridge thrust faults suggest a detachment with a significantly reduced basal friction coefficient.

The computed wedge angles ($\alpha + \beta$) vary between 1.2° and 2.2°. Smaller wedge angles mean that more deformation is taken up by the basal detachment or that the push stresses decrease, while larger wedge angles are indicative of stronger deformation of the wedge interior and/or enhanced push stresses. The wedge angles are highest but still very low for the stress centers C1 and C5, suggesting that during their activity horizontal stresses were possibly highest. Previously, Nahm and Schultz (2010) examined the topographic slopes of the Thaumasia Highlands against the inclinations necessitated by thrust faulting within a critical taper wedge framework. They concluded that the observed slopes, ranging from 0.418° to 1.017°, were not steep enough to indicate the deformation of the Martian lithosphere as a critical taper wedge. However, when considering the entire wedge length for computed centers, it becomes straightforward that larger wedge angles are achievable, with wrinkle ridge detachment depths varying between approximately 8.8 and 2.9 km. Schultz et al. (2010) proposed that the requisite conditions for the slip along a common basal décollement for critical taper wedge mechanics are hindered by three factors: the assumption that fluids come from profound depths, making it difficult for them to migrate along the decollement; and the adherence to models that depict wrinkle ridges as deep-seated basement uplifts. The depth of the detachments indicates a trend of becoming less deep as they move from the central region toward the periphery of the Tharsis dome, indicating that the concept of profound basement uplifts might not be the best fit. Nevertheless, the potential reasons for sliding along a shared basal detachment can be interpreted in terms of elements that might reduce the angle of internal friction. This will be elaborated upon in the subsequent section, where potential causative factors are discussed.

Equation 10 is used to calculate the internal friction angle as a function of the basal friction coefficient for detachments C1 to C5. These coefficients are individually calculated from wedge angles ($\alpha + \beta$). The lower internal friction angle means that the wedge would need to have a lower surface slope (assuming the basal friction angle stays the same) to maintain the balance of forces and mechanical equilibrium. This condition stems from the diminished capability of the wedge material to counteract the shear stress induced by the tectonic push. Our results are in agreement with that. Thus, for each corresponding function, a basal friction coefficient with a relatively low value is required. If the value of the internal friction angle can be considered constant for wedge angles, the basal friction coefficient, denoted as μ_b, is calculated as follows.

$$\alpha \approx \frac{1}{3}\mu_b - \frac{2}{3} \tag{11}$$

The basal friction coefficients related to the interface between each detachment and its underlying structure have been rigorously calculated and quantified as absolute values. This quantification process reflects the specific properties extending from C1 through C5. The resulting numerical outcomes for these basal friction coefficients μ_b are presented in Table 2 in a sequence corresponding to their respective detachments.

Another striking feature is that the topography and tilt angle of the basal detachment seem to correlate. Steeper topographic slopes in the periphery of Tharsis seem to correlate with a kink in the detachment toward a more flattish detachment. This circumstance underlines the interdependence of topography and wedge geometry.

The rise in the surface slope and the concomitant decrease in basal tilt could suggest an evolving state toward the magnitude and duration of the plume activity, variations in mechanical properties of the wedge and the detachment layer, or a combination of these factors. The superposition of linked wrinkle ridge segments of C3 and C4 shows that C4 has the youngest activity. This may indicate that the topography of the C4 may have not reached the mechanical equilibrium of the wedge.

5.4. The Potential Reasons Contributing to the Reduction of Friction Coefficient

The unusually low friction coefficients derived for the basal detachment require explanation. Generally, evaporates such as gypsum or halite may lubricate shear zones and effectively reduce the friction coefficients. Clay

minerals have the same effect. We suggest here in accordance with Karagoz et al. (2022a) that fluids at high lithostatic overpressure play a crucial role in the extremely weak basal detachment.

Although it may not be applicable to the region of interest in this study, the recent geophysical findings of the InSight mission indicate that the lithosphere of Mars exhibits discontinuities and is highly altered and/or fractured, ranging from approximately 8 to 11 km in depth (Lognonné et al., 2020). Knapmeyer-Endrun et al. (2021) suggests that the distribution of less resilient material might extend to depths of 6–11 km. This hypothesis is supported by evidence of phyllosilicate signatures and stratified low-density sedimentary rocks (Pan et al., 2020). Significantly, this concept is in agreement with the derived detachment depths and substantiates potential explanations for the reduction in the coefficient of friction. Karagoz et al. (2022a) showed that Martian geotherms cross the H_2O liquid-solid phase boundary at a depth matching with the detachments. Therefore, we propose that the detachment occurs at a depth where liquid water, rather than ice, is the stable phase. The nature of H_2O resides within the solid (ice) field in the calculated depth detachment and the cryospheric thickness may range from 0 to 9 km (Clifford et al., 2010). This condition effectively seals porous crustal structures, such as a mega-regolith, thereby rendering them an impenetrable permafrost layer. Besides, the conceptual climatic records from the Early Hesperian period indicate conditions that were warmer and more humid (Andrews-Hanna & Lewis, 2011) and chloride and perchlorate brines may have seeped downward, eventually freezing and formed an impermeable layer (Martínez & Renno, 2013). It is plausible that the upper megaregolith basement is largely impermeable to fluids. Upward migrating fluids from the liquid layer could also commence freezing, thereby sealing the rocks and contributing to the formation of permafrost below. Dohm, Ferris, et al. (2001) posited that the formation of a Tharsis basin could have been formed by evaporation and phyllosilicates, which were subsequently overlaid or inundated by multi-stages of Tharsis lavas. Wezel and Baioni (2010) presented evidence suggesting that the clastic structure of sulfate evaporite deposits in the Tithonium Chasma of the Valles Marineris region on Mars consists of a stratified succession with interbedded channel-fill breccia masses. These findings indicate subaqueous re-sedimentation of sulfate evaporites, hinting at their potential response to high denudation rates.

Another factor may be the serpentinization of the early Martian crust in the Noachian period (e.g., Chassefière et al., 2013; Quesnel et al., 2009) resulting from a predominant hydrothermal alteration process in the Tharsis basin, which may have caused the lowering of friction for basal detachments. The detachment's strength degradation escalates as the pore fluid pressure intensifies (Jaeger et al., 2007; Zoback, 2007). Hydrostatic fluid pressure is only present when fluids form a continuous network from the surface down to greater depths.

Consequently, the overlying formation applies lithostatic overburden to the fluid phase, generating a fluid overpressure at depth. This fluid pressure counterbalances the lithostatic stress (effective stress), leading to the material's yield strength being surpassed. The accumulation of fluid overpressure in the liquid layer, where the detachment is situated, may serve as a highly efficient mechanism to facilitate detachment faulting at the proposed detachment depths.

6. Conclusion

The comprehensive morphometric and kinematic analysis of 34,741 wrinkle ridge segments, which have a total length of 77,294 km, of the Tharsis rise enabled us to narrow down the stress history and temporal evolution of the Tharsis rise. We consider the Tharsis rise to represent a critical taper dome:

1. Superposed and crosscutting circum-Tharsis wrinkle ridges result from five different stress centers. These are labeled as C1 to C5. C1 is located at the southern edge of the Alba Mons caldera. C2 is found in Ceraunius Fossae. C3 is situated between Ulysses Patera and Pavonis Chasma. C4 is located at Phoenicis Lacus and C5 at Claritas Rupes.
2. Our results disclose multiple stages of activation for wrinkle ridges; however, the final stage of plume-induced stress is transmitted toward near Phoenicis Lacus.
3. Kinematic modeling of wrinkle ridges allows us to infer the amount of shortening and the reconstruction of the depth of a detachment, which ranges from ∼8.8–2.9 km. The amount of horizontal shortening was calculated for each center and the highest horizontal shortening on a radial topographic profile is 3.8 km for C4 and the lowest is 1.5 km for C1. The gently rising basal detachments and gently outward descending topography form a ∼4,500 km long acute shape, a circumferential wedge of 1.2°–2.2°. We apply the critical taper theory and infer a low basal friction coefficient for the basal detachment as a critical taper.

4. The computed results for the basal friction coefficient of each detachment from C1 to C5 are as follows: 0.077, 0.059, 0.055, 0.078, and 0.093. These values can be conceivably linked to the manifestation of fluid overpressure beneath stratigraphic units such as permafrost, salt layers, and clay layers.
5. Here, we propose that the reduction of the basal friction coefficient for detachments occurs in regions where liquid water, not ice, is the predominant stable phase. These formations could be conceivably linked to the manifestation of fluid overpressure beneath highly altered and/or fractured stratigraphic units such as salt layers, clay layers, evaporates, and permafrost. The upper crust functions as a permafrost layer, demonstrating impermeability to fluid transmission. Fluid overpressure, in this context, is regarded as a highly effective mechanism for substantially mitigating the basal friction coefficient along the detachment beneath the Tharsis dome.

Data Availability Statement

Data used in this paper, including the list of locations of all mapped wrinkle ridges and input files for concentric deviation computation, can be found in a repository following the FAIR principles (Karagoz et al., 2023).

Acknowledgments
We gratefully acknowledge the financial support of the scholarship grant of the Deutscher Akademischer Austauschdienst (DAAD) with a Grant of 57440921/91734694. The authors thank editor Laurent Montési and two anonymous reviewers for their very constructive and detailed comments and suggestions. Open Access funding enabled and organized by Projekt DEAL.

References

Anderson, R. C., Dohm, J. M., Golombek, M. P., Haldemann, A. F. C., Franklin, B. J., Tanaka, K. L., et al. (2001). Primary centers and secondary concentrations of tectonic activity through time in the western hemisphere of Mars. *Journal of Geophysical Research*, *106*(E9), 20563–20585. https://doi.org/10.1029/2000JE001278

Andrews-Hanna, J. C., & Broquet, A. (2023). The history of global strain and geodynamics on Mars. *Icarus*, *395*, 115476. https://doi.org/10.1016/j.icarus.2023.115476

Andrews-Hanna, J. C., & Lewis, K. W. (2011). Early Mars hydrology: 2. Hydrological evolution in the Noachian and Hesperian epochs. *Journal of Geophysical Research*, *116*(E2), E02007. https://doi.org/10.1029/2010JE003709

Baker, V. R., Maruyama, S., & Dohm, J. M. (2007). Tharsis superplume and the geological evolution of early Mars. *Superplumes: Beyond Plate Tectonics*, 507–522. https://doi.org/10.1007/978-1-4020-5750-2_16

Banerdt, W. B., Phillips, R. J., Sleep, N. H., & Saunders, R. S. (1982). Thick shell tectonics on one-plate planets: Applications to Mars. *Journal of Geophysical Research*, *87*(B12), 9723–9733. https://doi.org/10.1029/jb087ib12p09723

Bleacher, J. E., Greeley, R., Williams, D. A., Cave, S. R., & Neukum, G. (2007). Trends in effusive style at the Tharsis Montes, Mars, and implications for the development of the Tharsis province. *Journal of Geophysical Research*, *112*(9), E09005. https://doi.org/10.1029/2006JE002873

Bouley, S., Baratoux, D., Paulien, N., Missenard, Y., & Saint-Bézar, B. (2018). The revised tectonic history of Tharsis. *Earth and Planetary Science Letters*, *488*, 126–133. https://doi.org/10.1016/j.epsl.2018.02.019

Breuer, D., Yuen, D. A., Spohn, T., & Zhang, S. (1998). Three dimensional models of Martian mantle convection with phase transitions. *Geophysical Research Letters*, *25*(3), 229–232. https://doi.org/10.1029/97GL03767

Breuer, D., Zhou, H., Yuen, D. A., & Spohn, T. (1996). Phase transitions in the Martian mantle: Implications for the planet's volcanic history. *Journal of Geophysical Research*, *101*(E3), 7531–7542. https://doi.org/10.1029/96JE00117

Carr, M. H., & Head, J. W. (2010). Geologic history of Mars. *Earth and Planetary Science Letters*, *294*(3–4), 185–203. https://doi.org/10.1016/j.epsl.2009.06.042

Chassefière, E., Langlais, B., Quesnel, Y., & Leblanc, F. (2013). The fate of early Mars' lost water: The role of serpentinization. *Journal of Geophysical Research: Planets*, *118*(5), 1123–1134. https://doi.org/10.1002/jgre.20089

Clifford, S. M., Lasue, J., Heggy, E., Boisson, J., McGovern, P., & Max, M. D. (2010). Depth of the Martian cryosphere: Revised estimates and implications for the existence and detection of subpermafrost groundwater. *Journal of Geophysical Research*, *115*(E7), E07001. https://doi.org/10.1029/2009je003462

Dahlen, F. A. (1990). Critical taper model of fold-and-thrust belts and accretionary wedges. *Annual Review of Earth and Planetary Sciences*, *18*(1), 55–99. https://doi.org/10.1146/annurev.ea.18.050190.000415

Dohm, J. M., Anderson, R. C., Barlow, N. G., Miyamoto, H., Davies, A. G., Taylor, G. J., et al. (2008). Recent geological and hydrological activity on Mars: The Tharsis/Elysium corridor. *Planetary and Space Science*, *56*(7), 985–1013. https://doi.org/10.1016/jpss200801001

Dohm, J. M., Baker, V. R., Maruyama, S., & Anderson, R. C. (2007). Traits and evolution of the Tharsis superplume, Mars. *Superplumes: Beyond plate tectonics*, 523–536. https://doi.org/10.1007/978-1-4020-5750-2_17

Dohm, J. M., Ferris, J. C., Baker, V. R., Anderson, R. C., Hare, T. M., Strom, R. G., et al. (2001). Ancient drainage basin of the Tharsis region, Mars: Potential source for outflow channel systems and putative oceans or paleolakes. *Journal of Geophysical Research*, *106*(E12), 32943–32958. https://doi.org/10.1029/2000JE001468

Dohm, J. M., & Tanaka, K. L. (1999). Geology of the Thaumasia region, Mars: Plateau development, valley origins, and magmatic evolution. *Planetary and Space Science*, *47*(3–4), 411–431. https://doi.org/10.1016/S0032-0633(98)00141-X

Dohm, J. M., Tanaka, K. L., & Hare, T. M. (2001). Geologic map of the Thaumasia region of Mars. *Assemblage*, *2*(5), 16.

Dohm, J. M., Williams, J. P., Anderson, R. C., Ruiz, J., McGuire, P. C., Komatsu, G., et al. (2009). New evidence for a magmatic influence on the origin of Valles Marineris, Mars. *Journal of Volcanology and Geothermal Research*, *185*(1–2), 12–27. https://doi.org/10.1016/j.jvolgeores.2008.11.029

Dongmo Wamba, M., Montagner, J. P., & Romanowicz, B. (2023). Imaging deep-mantle plumbing beneath La Réunion and Comores hot spots: Vertical plume conduits and horizontal ponding zones. *Science Advances*, *9*(4), eade3723. https://doi.org/10.1126/sciadv.ade3723

Edwards, C. S., Nowicki, K. J., Christensen, P. R., Hill, J., Gorelick, N., & Murray, K. (2011). Mosaicking of global planetary image datasets: 1. Techniques and data processing for thermal emission imaging system (THEMIS) multi-spectral data. *Journal of Geophysical Research*, *116*(E10), E10008. https://doi.org/10.1029/2010JE003755

Fergason, R. L., Hare, T. M., & Laura, J. (2018). *HRSC and MOLA blended digital elevation model at 200m v2. Astrogeology PDS Annex*. US Geological Survey.

Frey, H., Lowry, B. L., & Chase, S. A. (1979). Pseudocraters on Mars. *Journal of Geophysical Research*, *84*(B14), 8075–8086. https://doi.org/10.1029/jb084ib14p08075

Harder, H., & Christensen, U. R. (1996). A one-plume model of Martian mantle convection. *Nature*, *380*(6574), 507–509. https://doi.org/10.1038/380507a0

Hartmann, W. K. (1973). Martian surface and crust: Review and synthesis. *Icarus*, *19*(4), 550–575. https://doi.org/10.1016/0019-1035(73)90083-3

Hauber, E., Brož, P., Jagert, F., Jodowski, P., & Platz, T. (2011). Very recent and wide-spread basaltic volcanism on Mars. *Geophysical Research Letters*, *38*(10), L10201. https://doi.org/10.1029/2011GL047310

Head, J. W., Kreslavsky, M. A., & Stephen, P. (2002). Northern lowlands of Mars: Evidence for widespread volcanic flooding and tectonic deformation in the Hesperian Period. *Journal of Geophysical Research*, *107*(E1), 5003. https://doi.org/10.1029/2000JE001445

Hynek, B. M., Robbins, S. J., Šrámek, O., & Zhong, S. J. (2011). Geological evidence for a migrating Tharsis plume on early Mars. *Earth and Planetary Science Letters*, *310*(3–4), 327–333. https://doi.org/10.1016/j.epsl.2011.08.020

Jaeger, J. C., Cook, N. G. W., & Zimmerman, R. (2007). *Fundamentals of rock mechanics* (p. 475). Blackwell.

Janle, P., & Erkul, E. (1991). Gravity studies of the Tharsis area on Mars. *Earth, Moon, and Planets*, *53*(3), 217–232. https://doi.org/10.1007/bf00055948

Johnson, C. L., & Phillips, R. J. (2005). Evolution of the Tharsis region of Mars: Insights from magnetic field observations. *Earth and Planetary Science Letters*, *230*(3–4), 241–254. https://doi.org/10.1016/j.epsl.2004.10.038

Karagoz, O., Kenkmann, T., & Hergarten, S. (2023). Dataset: Unraveling the tectonic history of the Tharsis rise on Mars: Plume migration and critical taper dome. *Journal of Geophysical Research: Planets*. https://doi.org/10.5281/zenodo.8061711

Karagoz, O., Kenkmann, T., & Wulf, G. (2022a). Circum-Tharsis wrinkle ridges at Lunae Planum: Morphometry, formation, and crustal implications. *Icarus*, *374*, 114808. https://doi.org/10.1016/j.icarus.2021.114808

Karagoz, O., Kenkmann, T., & Wulf, G. (2022b). Insights into the subsurface structure of wrinkle ridges on Mars. *Earth and Planetary Science Letters*, *595*, 117759. https://doi.org/10.1016/j.epsl.2022.117759

Keller, T., & Tackley, P. J. (2009). Towards self-consistent modeling of the Martian dichotomy: The influence of one-ridge convection on crustal thickness distribution. *Icarus*, *202*(2), 429–443. https://doi.org/10.1016/j.icarus.2009.03.029

Kenkmann, T., Vasconcelos, M. A. R., Crósta, A. P., & Reimold, W. U. (2011). The complex impact structure Serra da Cangalha, Tocantins State, Brazil. *Meteoritics & Planetary Sciences*, *46*(6), 875–889. https://doi.org/10.1111/j.1945-5100.2011.01199.x

Kiefer, W. S. (2003). Melting in the Martian mantle: Shergottite formation and implications for present-day mantle convection on Mars. *Meteoritics & Planetary Sciences*, *38*(12), 1815–1832. https://doi.org/10.1111/j.1945-5100.2003.tb00017.x

Knapmeyer, M., Oberst, J., Hauber, E., Wählisch, M., Deuchler, C., & Wagner, R. (2006). Working models for spatial distribution and level of Mars' seismicity. *Journal of Geophysical Research*, *111*(11), 1–23. https://doi.org/10.1029/2006JE002708

Knapmeyer, M., Schneider, S., Misun, M., Wählisch, M., & Hauber, E. (2008). An extended global inventory of Mars surface faults. *Geophysical Research Abstracts*, *10*(EGU2008-A-03574), 11006.

Knapmeyer-Endrun, B., Panning, M. P., Bissig, F., Joshi, R., Khan, A., Kim, D., et al. (2021). Thickness and structure of the Martian crust from InSight seismic data. *Science*, *373*(6553), 438–443. https://doi.org/10.1126/science.abf8966

Leone, G. (2016). Alignments of volcanic features in the southern hemisphere of Mars produced by migrating mantle plumes. *Journal of Volcanology and Geothermal Research*, *309*, 78–95. https://doi.org/10.1016/j.jvolgeores.2015.10.028

Lognonné, P., Banerdt, W. B., Pike, W. T., Giardini, D., Christensen, U., Garcia, R. F., et al. (2020). Constraints on the shallow elastic and anelastic structure of Mars from InSight seismic data. *Nature Geoscience*, *13*(3), 213–220. https://doi.org/10.1038/s41561-020-0536-y

Mangold, N., Allemand, P., & Thomas, P. G. (1998). Wrinkle ridges of Mars: Structural analysis and evidence for shallow deformation controlled by ice-rich décollements. *Planetary and Space Science*, *46*(4), 345–356. https://doi.org/10.1016/s0032-0633(97)00195-5

Mangold, N., Allemand, P., Thomas, P. G., & Vidal, G. (2000). Chronology of compressional deformation on Mars: Evidence for a single and global origin. *Planetary and Space Science*, *48*(12–14), 1201–1211. https://doi.org/10.1016/S0032-0633(00)00104-5

Martínez, G. M., & Renno, N. O. (2013). Water and brines on Mars: Current evidence and implications for MSL. *Space Science Reviews*, *175*(1–4), 29–51. https://doi.org/10.1007/s11214-012-9956-3

Mège, D., & Masson, P. (1996a). A plume tectonics model for the Tharsis province, Mars. *Planetary and Space Science*, *44*(12), 1499–1546. https://doi.org/10.1016/S0032-0633(96)00113-4

Mège, D., & Masson, P. (1996b). Stress models for Tharsis formation, Mars. *Planetary and Space Science*, *44*(12), 1471–1497. https://doi.org/10.1016/s0032-0633(96)00112-2

Montési, L. G. J., & Zuber, M. T. (2003). Spacing of faults at the scale of the lithosphere and localization instability: 2. Application to the central Indian basin. *Journal of Geophysical Research*, *108*(B2), 1–16. https://doi.org/10.1029/2002jb001924

Nahm, A. L., & Schultz, R. A. (2010). Evaluation of the orogenic belt hypothesis for the formation of the Thaumasia Highlands, Mars. *Journal of Geophysical Research*, *115*(E4), E04008. https://doi.org/10.1029/2009je003327

Nimmo, F., & Tanaka, K. (2005). Early crustal evolution of Mars. *Annual Review of Earth and Planetary Sciences*, *33*(1), 133–161. https://doi.org/10.1146/annurev.earth.33.092203.122637

Okubo, C. H., & Schultz, R. A. (2004). Mechanical stratigraphy in the western equatorial region of Mars based on thrust fault-related fold topography and implications for near-surface volatile reservoirs. *Bulletin of the Geological Society of America*, *116*(5–6), 594–605. https://doi.org/10.1130/B25361.1

Pan, L., Quantin-Nataf, C., Tauzin, B., Michaut, C., Golombek, M., Lognonné, P., et al. (2020). Crust stratigraphy and heterogeneities of the first kilometers at the dichotomy boundary in western Elysium Planitia and implications for InSight lander. *Icarus*, *338*, 113511. https://doi.org/10.1016/j.icarus.2019.113511

Phillips, R. J., Zuber, M. T., Solomon, S. C., Golombek, M. P., Jakosky, B. M., Banerdt, W. B., et al. (2001). Ancient geodynamics and global-scale hydrology on Mars. *Science*, *291*(5513), 2587–2591. https://doi.org/10.1126/science.1058701

Plescia, J. B. (2004). Morphometric properties of Martian volcanoes. *Journal of Geophysical Research*, *109*(3), E03003. https://doi.org/10.1029/2002je002031

Poelchau, M. H., & Kenkmann, T. (2008). Asymmetric signatures in simple craters as an indicator for an oblique impact vector. *Meteoritics & Planetary Sciences*, *43*(12), 2059–2072. https://doi.org/10.1111/j.1945-5100.2008.tb00661.x

Quesnel, Y., Sotin, C., Langlais, B., Costin, S., Mandea, M., Gottschalk, M., & Dyment, J. (2009). Serpentinization of the Martian crust during Noachian. *Earth and Planetary Science Letters*, *277*(1–2), 184–193. https://doi.org/10.1016/j.epsl.2008.10.012

Richardson, J. A., Bleacher, J. E., Connor, C. B., & Glaze, L. S. (2021). Small volcanic vents of the Tharsis volcanic province, Mars. *Journal of Geophysical Research: Planets*, *126*(2), e2020JE006620. https://doi.org/10.1029/2020JE006620

Robbins, S. J., Di Achille, G., & Hynek, B. M. (2011). The volcanic history of Mars: High-resolution crater-based studies of the calderas of 20 volcanoes. *Icarus*, *211*(2), 1179–1203. https://doi.org/10.1016/j.icarus.2010.11.012

Robbins, S. J., Kirchoff, M. R., & Hoover, R. H. (2023). Fully controlled 6 meters per pixel equatorial mosaic of Mars from Mars Reconnaissance Orbiter Context Camera images, version 1. *Earth and Space Science*, *10*(3), e2022EA002443. https://doi.org/10.1029/2022ea002443

Roberts, J. H., & Zhong, S. (2006). Degree-1 convection in the Martian mantle and the origin of the hemispheric dichotomy. *Journal of Geophysical Research*, *111*(6), E06013. https://doi.org/10.1029/2005JE002668

Saffer, D. M., & Bekins, B. A. (2006). An evaluation of factors influencing pore pressure in accretionary complexes: Implications for taper angle and wedge mechanics. *Journal of Geophysical Research*, *111*(B4), B04101. https://doi.org/10.1029/2005JB003990

Schultz, R., Nahm, A., & Montési, L. (2010). Wrinkle ridges on Mars: Absence of décollement tectonics. In *EGU general assembly conference abstracts* (p. 1969).

Schultz, R. A. (1985). Assessment of global and regional tectonic models for faulting in the ancient terrains of Mars. *Journal of Geophysical Research*, *90*(B9), 7849–7860. https://doi.org/10.1029/JB090iB09p07849

Schultz, R. A. (2000). Localization of bedding plane slip and backthrust faults above blind thrust faults: Keys to wrinkle ridge structure. *Journal of Geophysical Research*, *105*(E5), 12035–12052. https://doi.org/10.1029/1999JE001212

Scott, D. H., & Tanaka, K. L. (1986). Geologic map of the western equatorial region of Mars, scale 1:15,000,000. In *U.S. Geological Survey Map I-1802-A*. (Vol. 1). Geological Survey (US). Retrieved from http://astrogeology.usgs.gov/Projects/PlanetaryMapping/DIGGEOL/mars/marswest/mw.pdf%5Cnpapers3://publication/uuid/9DE8930B-BC79-41A2-98E9-42D39A4380EF

Sleep, N. H., & Phillips, R. J. (1985). Gravity and lithospheric stress on the terrestrial planets with reference to the Tharsis Region of Mars. *Journal of Geophysical Research*, *90*(B6), 4469–4489. https://doi.org/10.1029/JB090iB06p04469

Smith, D. E., Zuber, M. T., Frey, H. V., Garvin, J. B., Head, J. W., Muhleman, D. O., et al. (2001). Mars orbiter laser altimeter: Experiment summary after the first year of global mapping of Mars. *Journal of Geophysical Research*, *106*(E10), 23689–23722. https://doi.org/10.1029/2000JE001364

Solomon, S. C., Aharonson, O., Aurnou, J. M., Banerdt, W. B., Carr, M. H., Dombard, A. J., et al. (2005). New perspectives on ancient Mars. *Science*, *307*(5713), 1214–1220. https://doi.org/10.1126/science.1101812

Solomon, S. C., & Head, J. W. (1980). Lunar mascon basins: Lava filling, tectonics, and evolution of the lithosphere. *Reviews of Geophysics*, *18*(1), 107–141. https://doi.org/10.1029/RG018i001p00107

Solomon, S. C., & Head, J. W. (1982). Evolution of the Tharsis Province of Mars: The importance of heterogeneous lithospheric thickness and volcanic construction. *Journal of Geophysical Research*, *87*(B12), 9755–9774. https://doi.org/10.1029/jb087ib12p09755

Suppe, J., & Connors, C. (1992). Critical taper wedge mechanics of fold-and-thrust belts on Venus: Initial results from Magellan. *Journal of Geophysical Research*, *97*(E8), 13545–13561. https://doi.org/10.1029/92je01164

Suppe, J., & Medwedeff, D. A. (1990). Geometry and kinematics of fault-propagation folding. *Eclogae Geologicae Helvetiae*, *83*(3), 409–454.

Tanaka, K. L., Golombek, M. P., & Banerdt, W. B. (1991). Reconciliation of stress and structural histories of the Tharsis region of Mars. *Journal of Geophysical Research*, *96*(E1), 15617–15633. https://doi.org/10.1029/91JE01194

Thurber, C. H., & Toksöz, M. N. (1978). Martian lithospheric thickness from elastic flexure theory. *Geophysical Research Letters*, *5*(11), 977–980. https://doi.org/10.1029/GL005i011p00977

von Hagke, C., Oncken, O., & Evseev, S. (2014). Critical taper analysis reveals lithological control of variations in detachment strength: An analysis of the Alpine basal detachment (Swiss Alps). *Geochemistry, Geophysics, Geosystems*, *15*(1), 176–191. https://doi.org/10.1002/2013GC005018

Watters, T. R. (1988). Wrinkle ridge assemblages on the terrestrial planets. *Journal of Geophysical Research*, *93*(B9), 10236–10254. https://doi.org/10.1029/JB093iB09p10236

Watters, T. R. (1993). Compressional tectonism on Mars. *Journal of Geophysical Research*, *98*(E9), 17049–17060. https://doi.org/10.1029/93JE01138

Watters, T. R. (2004). Elastic dislocation modeling of wrinkle ridges on Mars. *Icarus*, *171*(2), 284–294. https://doi.org/10.1016/j.icarus.2004.05.024

Watters, T. R., & Maxwell, T. A. (1983). Crosscutting relations and relative ages of ridges and faults in the Tharsis region of Mars. *Icarus*, *56*(2), 278–298. https://doi.org/10.1016/0019-1035(83)90039-8

Watters, T. R., & Maxwell, T. A. (1986). Orientation, relative age, and extent of the Tharsis Plateau ridge system. *Journal of Geophysical Research*, *91*(B8), 8113–8125. https://doi.org/10.1029/JB091iB08p08113

Wenzel, M. J., Manga, M., & Jellinek, A. M. (2004). Tharsis as a consequence of Mars' dichotomy and layered mantle. *Geophysical Research Letters*, *31*(4), L04702. https://doi.org/10.1029/2003gl019306

Wezel, F. C., & Baioni, D. (2010). Evidence for subaqueously resedimented sulphate evaporites on Mars. *Planetary and Space Science*, *58*(11), 1500–1505. https://doi.org/10.1016/j.pss.2010.07.003

Willemann, R. J., & Turcotte, D. L. (1982). The role of lithospheric stress in the support of the Tharsis Rise. *Journal of Geophysical Research*, *87*(B12), 9793–9801. https://doi.org/10.1029/jb087ib12p09793

Wise, D. U., Golombek, M. P., & McGill, G. E. (1979). Tharsis province of Mars: Geologic sequence, geometry, and a deformation mechanism. *Icarus*, *38*(3), 456–472. https://doi.org/10.1016/0019-1035(79)90200-8

Yin, A., & Wang, Y. (2023). Formation and modification of wrinkle ridges in the central Tharsis region of Mars as constrained by detailed geomorphological mapping and landsystem analysis. *Earth and Planetary Physics*, *7*(2), 161–192. https://doi.org/10.26464/epp2023031

Zhong, S. (2009). Migration of Tharsis volcanism on Mars caused by differential rotation of the lithosphere. *Nature Geoscience*, *2*(1), 19–23. https://doi.org/10.1038/ngeo392

Zhong, S., & Zuber, M. T. (2001). Degree-1 mantle convection and the crustal dichotomy on Mars. *Earth and Planetary Science Letters*, *189*(1–2), 75–84. https://doi.org/10.1016/S0012-821X(01)00345-4

Zoback, M. D. (2007). *Reservoir geomechanics* (Vol. 489). Cambridge University Press. https://doi.org/10.1017/CBO9780511586477